11 Convective Storms and Cloud Dynamics

Convective precipitation originates from cumulus clouds, namely Cu con and Cb (Table 1.1, Figure 1.4b and Chapter 10). In cumulus clouds, hydrometeors grow to precipitation size in a short time, usually within 20–30 minutes. This is most efficiently achieved in Cb, which consists of water and ice and has the largest vertical extent and highest vertical velocities of all clouds (Table 1.3). Cb clouds are the building blocks of all convective storms and will be discussed first (Section 11.1). Even though traditionally all convective storms are referred to as thunderstorms, we go along with the nomenclature by Bluestein (2013) and refer to these as convective storms because it is possible for convective storms to not produce thunder and lightning.

The various types of convective storms can generally be grouped into three categories (Table 11.1):

1. *Ordinary-cell convective storms*, for brevity ordinary-cells, also referred to as isolated, single-cell, or pulse thunderstorms. They consist of only a single convective cell and last approximately 30–60 min (Miller and Mote, 2017).
2. *Multicell convective storms*[1], also referred to as multicellular clusters, for brevity multicells. They consist of several ordinary convective cells[2] in different stages of development. While each cell lasts typically 30–60 min, the entire multicell storm may last for several hours.
3. Supercell convective storms[3], for brevity supercells. They consist of only one large self-maintaining convective cell and also last several hours.

Supercells are the rarest type of convective storms, but the most violent. Whether a given convective storm turns out to be an ordinary cell (Section 11.1), multicell, or supercell storm (Section 11.2) depends on both the vertical shear of the horizontal wind $\vec{v}_h$ in the environment (hereafter just referred to as the vertical wind shear) and the static stability of the atmosphere.

The above-mentioned convective storms can cluster together in larger entities, called *mesoscale convective systems* (MCSs) (Maddox, 1980; Houze and Hobbs, 1982; Houze Jr., 1989) as will be discussed in Section 11.3. Cb clouds have the potential to turn into thunderstorms, owing to the co-existence of water and ice, which is a prerequisite for the formation of lightning and thunder (Section 11.4). Tropical cyclones, which are also classified as MCSs will be discussed in terms of their formation, intensification, and transition into extratropical cyclones in Section 11.5. This chapter ends with a discussion of the observed changes in tropical and extratropical cyclones in the last decades and projected future changes (Section 11.6).

[1] https://glossary.ametsoc.org/wiki/Multicell_convective_storm
[2] https://glossary.ametsoc.org/wiki/Ordinary_cell
[3] https://glossary.ametsoc.org/wiki/Supercell

https://doi.org/10.1017/9781009485654.012 Published online by Cambridge University Press

Table 11.1 Summary of characteristics for ordinary-cell, multicell, and supercell convective storms. The values have been taken from Markowski and Richardson (2010) if not indicated otherwise.

	Ordinary-cell	Multicell	Supercell
Lifetime	30–60 min[a]	Several hours	1–4 h common, 8 h possible
Horizontal extent	8–16 km	20–25 km[b]	Mesocyclone: 3–8 km; supercell: 30 to >50 km[c]
Updraft speed	5 m s^{-1} to > 40 m s^{-1}		10–50 m s^{-1}[d]
Vertical wind shear between 0 and 6 km	Weak (<10 m s^{-1})	Moderate, unidirectional (8–21 m s^{-1})	Strong, turning (>18 m s^{-1})
CAPE	Hundreds to >2000 J kg^{-1}	>6000 J kg^{-1} possible[e]	>6000 J kg^{-1} possible[f]
Tornadoes		Weak ones possible[g]	Strong to violent ones possible
Equivalent radius of hailstones	<2.5 cm	>1 cm[h]	>2.5 cm[i]
Lightning rate	2–10 min^{-1}	1–60 min^{-1}[j]	2–100 min^{-1}[k]

[a]Miller and Mote (2017), [b]Houze (2014), [c]Markowski et al. (2018), [d]Houze (2014); Marinescu et al. (2020), [e]Avolio and Miglietta (2022), [f]Markowski et al. (2018), [g]Avolio and Miglietta (2022), [h]Raupach et al. (2021), [i]Smith et al. (2012); Blair et al. (2017), [j]Carey et al. (2019), [k]Houze (2014); Carey et al. (2019)

11.1 Ordinary-Cell Convective Storms

An ordinary-cell convective storm is also called a *pulse storm* (Miller and Mote, 2017) because of its short lifetime (Table 1.3) and because it may generate another ordinary-cell in another location. The latter takes place if its cold air outflow at Earth' surface causes sufficient lifting of warm air to reach the LFC. Thus, this type of ordinary convective storm occurs in pulses. It undergoes a characteristic life cycle and is often accompanied by graupel and hail formation.

A typical life cycle of an ordinary convective storm can be characterized by three main stages (Byers and Braham, 1948; Byers, 1949; Emanuel, 1994), shown in Figure 11.1. The early (cumulus) stage is characterized by vigorous updrafts of buoyant air parcels that form in a statically unstable or conditionally unstable atmosphere. These updrafts, associated with high supersaturations and a large water vapor supply, set the stage for the rapid growth of liquid hydrometeors due to collision–coalescence (Section 8.2), as well as ice microphysical processes including rapid growth by riming, above the 0 °C isotherm (Section 9.3). The temperature is higher inside the updraft than in the surrounding environment because of the latent heat released by condensation and freezing, as illustrated in Figure 11.1 for the 0 °C isotherm, which is at a higher altitude inside the updraft of the cloud than outside the cloud. In the early stage, the cumulus cloud is not yet precipitating.

https://doi.org/10.1017/9781009485654.012 Published online by Cambridge University Press

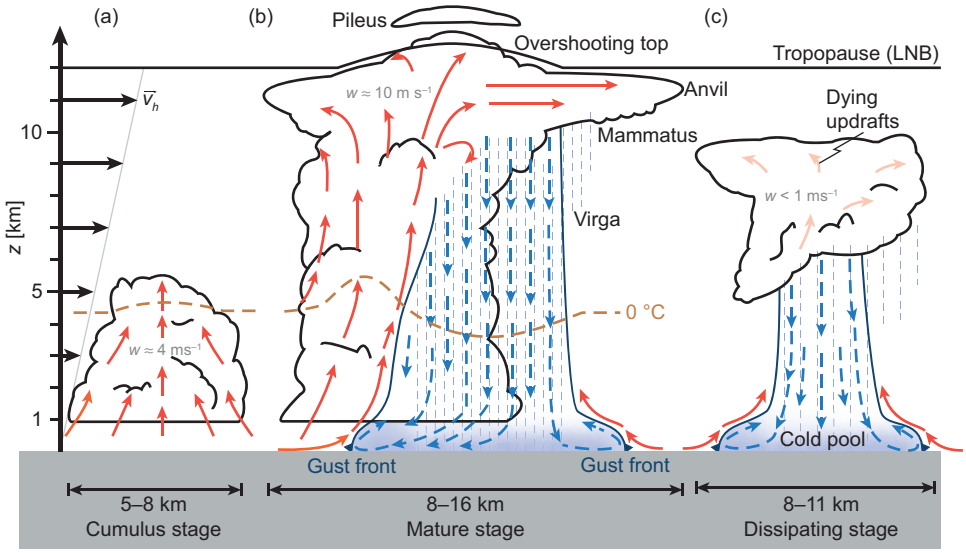


Figure 11.1 Cross section of the three main stages in the life cycle of an isolated ordinary convective storm with typical updraft speeds w: (a) cumulus (congestus) stage, (b) mature (Cb) stage, and (c) dissipating (stratiform) stage. The red and blue arrows denote the air motion associated with updrafts and downdrafts, respectively, and the black arrows along the vertical axis represent the strength of the horizontal wind $\vec{v}_h$. The thin solid lines in (b) and (c) enclosing vertical broken lines represent the boundary of the precipitation-cooled air and the warmer air masses, forming a gust front at the surface. The updraft speeds correspond to those in Table 1.3. Adapted from Doswell (1985).

The mature stage is governed by strong updrafts within the cloud and downdrafts associated with a heavy downpour of precipitation (Figure 11.1b). The downdrafts can either coincide with the updrafts or be slightly displaced horizontally. A horizontal displacement between the updrafts and the downdrafts is indicative of vertical wind shear, as illustrated in Figure 11.1. In the mature phase of the convective storm, the updrafts are most vigorous, and the 0 °C isotherm is displaced even higher in the updraft region. The updraft speeds are highest in the center of the cloud, where it is not influenced by entrainment (Section 5.2.6). Here, the updrafts slightly surpass the LNB (Section 5.2), as indicated by the overshooting top in the middle of the cloud top in Figure 11.1b. LNB is reached at the temperature inversion of the tropopause, indicated in Figure 11.1 at 12 km altitude, a typical tropopause height in midlatitudes. The stably stratified air above the LNB acts like a lid, which causes the overshooting air to experience a downward restoring force. The air then spreads out horizontally, forming the anvil. If the anvil forms below the tropopause, it consists of ice crystals and is also called *anvil cirrus*.

Overshooting air is sometimes visible in the form of a pileus, or cap cloud, which is a small horizontal lenticularis cloud (Section 1.2.3, Figures 4.1 and 11.1b) that forms on top of the convective cloud, when humid air is vertically displaced ahead of a rising thermal (Garrett et al., 2006). A pileus cloud is typically much thinner than the anvil. The pileus cloud can be a harbinger of severe weather and can mark the transition of a Cu con into a Cb (Figure 1.6).

https://doi.org/10.1017/9781009485654.012 Published online by Cambridge University Press

In the mature stage of the ordinary convective storm, precipitation falls from the majority of the cloud and extends all the way to Earth' surface (Figure 11.1b). Where the air is dry underneath the anvil, the hydrometeors sublimate, and a virga can be observed (Chapter 1). Sometimes also mammatus clouds (Figure 1.11c) are visible. Falling precipitation causes a downward drag as indicated by the blue broken arrows in Figure 11.1. The 0 °C isotherm extends to lower altitudes in the downdrafts because of latent heat consumption due to the melting of frozen hydrometeors. Depending on the RH, further cooling of the air within the downdraft region is caused by evaporation of hydrometeors below cloud base. The cold air pouch developing below the cloud is called a *cold pool* (e.g., Böing et al., 2012; Schlemmer and Hohenegger, 2014). The boundary between the cold air and the warmer air at Earth's surface is called a *gust front* (Figure 11.1b). The gust front is an example of a density current: the air from the cloud outflow (behind the gust front) is cold and dense and pushes the warmer environmental air (ahead of the gust front) out of its way as it spreads out and propagates horizontally along the surface. Here, behind and ahead denote the directions relative to the movement of the gust front. The larger the density gradient between the cold and warm air masses, the faster the gust front propagates. The gust front is accompanied by locally strong wind gusts: it initiates strong upward air motion ahead of it and directly behind it, followed by a turbulent wake (Droegemeier and Wilhelmson, 1987; Mahoney, 1988).

The downdrafts that cause gust fronts are classified according to their horizontal extent. If the horizontal extent is less than 10 km and the diverging wind speeds exceed $10\,\mathrm{m\,s^{-1}}$, the downdrafts are known as downbursts (Markowski and Richardson, 2010). Downbursts are divided into microbursts, which last between 1 and 5 min in an area of less than 4 km, and macrobursts, which cover an area between 4 and 10 km and last between 5 and 30 min (Wakimoto, 1985).

In the case of an ordinary convective storm, in which the environmental vertical wind shear is low, the inflow of air into the storm is too weak to provide resistance to the dense cold pool and to restrain the gust front from spreading out along the surface. Once the cold air spreads out horizontally underneath the convective storm, it starts to cut off the supply of warm air for the updraft. This terminates the mature stage and causes the ordinary convective storm to turn into its dissipating stage, where only downdrafts can exist (Figure 11.1c). The convective storm still precipitates in the dissipating stage, but the intensity of precipitation is weaker than during the mature stage. The anvil with its virga now extends to lower altitudes because of the pre-moistened air from previously sublimated frozen hydrometeors and evaporated rain drops. In the dissipating stage, the cloud and the precipitation take on a stratiform character (Houze, 1997).

An example of a radiosonde profile from a convective storm in Payerne, Switzerland is shown in Figure 11.2. The LCL (Figure 5.5) was at 790 hPa, the LFC at 710 hPa, and the LNB at 260 hPa. It had a CAPE value of $565\,\mathrm{J\,kg^{-1}}$, corresponding to weak to moderate convection (Table 5.1). The vertical wind shear in the lowest 6 km was $7.6\,\mathrm{m\,s^{-1}}$, deduced from the wind barbs on the right-hand side of Figure 11.2. The wind speed is given by the colors of the barbs. The wind direction is given by the orientation of the wind barbs, with the wind blowing in the direction of the arrow. In our example, the wind speed at 10 m above ground is

https://doi.org/10.1017/9781009485654.012 Published online by Cambridge University Press

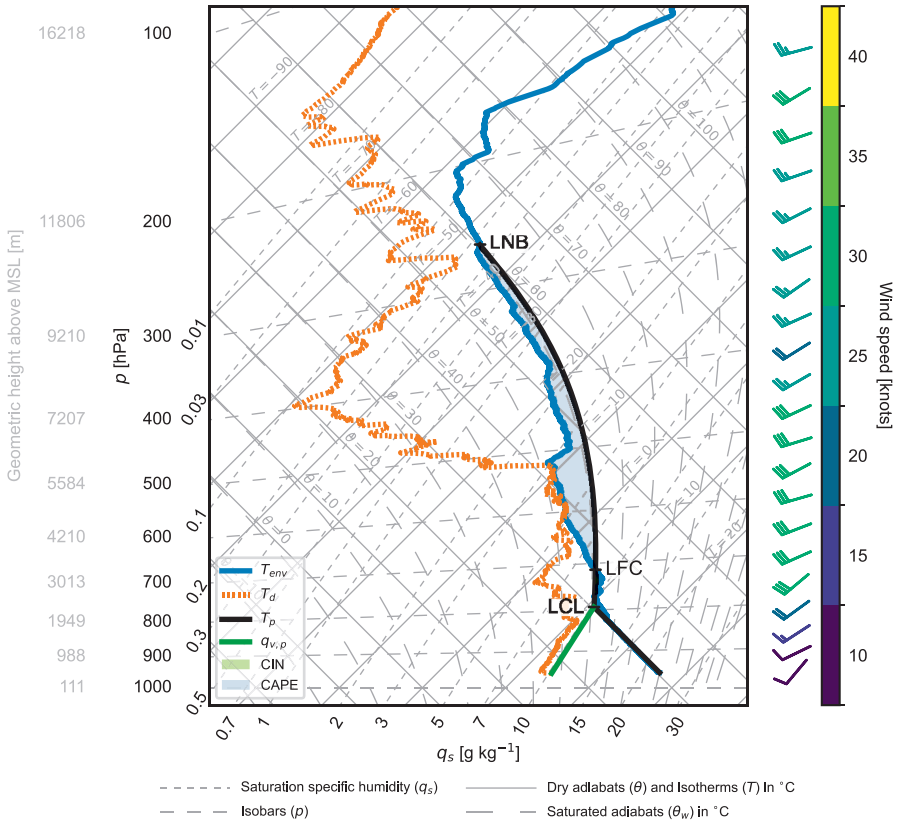


Figure 11.2 Profiles of T_{env} (blue), T_d (orange dashed), and wind barbs (right color bar) in a tephigram in an environment where ordinary convective storms formed. The sounding was taken in Payerne, Switzerland on July 10, 2020 at 11:00 local time. Overlaid is an air parcel ascent (black and green lines). The wind barbs at the right-hand side of the tephigram indicate wind direction and speed. The arrow direction corresponds to the direction the wind is coming from; the barbed end points in the direction the wind is coming from. The lines along the wind barbs indicate the wind speeds in knots (1 knot $= 1.852\,\mathrm{km\,h^{-1}} = 0.514\,\mathrm{m\,s^{-1}}$) short barb: 5 knots; long barb: 10 knots; pennants: 50 knots. CAPE denotes the convectively available potential energy and CIN the convective inhibition. Sounding data were obtained from http://weather.uwyo.edu/upperair/bufrraob.shtml.

$5.2\,\mathrm{m\,s^{-1}}$ and increased to $12.8\,\mathrm{m\,s^{-1}}$ at 6 km above ground. Thus, this sounding is typical of weak ordinary cell convection.

11.2 Multicell and Supercell Convective Storms

Ordinary-cell convective storms can also occur in larger clusters and be part of a bigger cloud system. There are two types of larger storms, namely multicell and supercell storms. A multicell storm consists of multiple ordinary convective cells in different stages of development,

https://doi.org/10.1017/9781009485654.012 Published online by Cambridge University Press

that can produce small to moderate size hailstones, typically less than 1.75 cm in radius (Raupach et al., 2021, Table 11.1), and may produce weak tornadoes (Avolio and Miglietta, 2022) (Section 11.2.5). By contrast, a supercell storm consists of one large cell. It tends to produce the largest hailstones (>2.5 cm in radius; Smith et al., 2012; Blair et al., 2017, Table 11.1) and the most violent tornadoes (Trapp et al., 2005a), see Section 11.2.5. A key to the longevity and strength of both multicell and supercell storms as compared to ordinary convective storms is their stronger vertical wind shear (Figure 11.3 and Table 11.1). This vertical wind shear ensures that the updraft and downdraft regions within the convective cells are horizontally displaced. Therefore, the area of the heaviest precipitation, that is, the downdraft, is separated from that of the updraft and does not shut it off.

Figure 11.3 shows simulation results from a three-dimensional cloud model (Weisman and Klemp, 1982) of the maximum updraft speed as a function of time for different values of the vertical wind shear. In the case of no vertical wind shear (ordinary convective storm), the maximum updraft speed, 40 m s^{-1}, is reached after 25 min and the storm decays after 50 min. This is in good agreement with observations of the lifetime of ordinary convective storms (Table 11.1).

Multicell storms typically have moderate vertical wind shears of around 8–21 m s^{-1} in the lowest 6 km. This allows the gust front to remain within the storm system and to repeatedly trigger new cells. As shown in Figure 11.3, simulations for a 15 m s^{-1} vertical wind shear show a first maximum in vertical velocity after 25 min, with new maxima appearing after 85 and 110 min.

Supercells require strong vertical wind shear of more than 18 m s^{-1} in the lowest 6 km (Table 11.1). In addition to the prerequisite of strong vertical wind shear, it is important that the

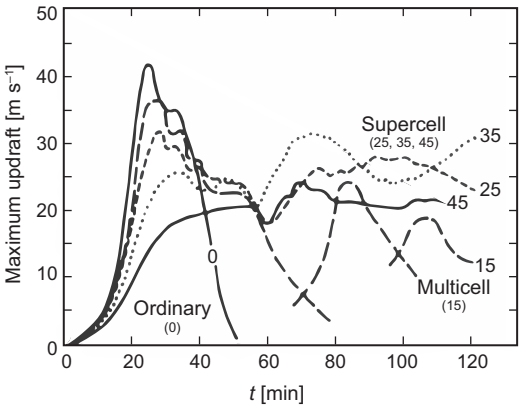


Figure 11.3 Maximum updraft speeds as a function of time for ordinary, multicell, and supercell convective storms. The lines are labeled in m s^{-1} according to the vertical wind shear between the surface and 6 km height. Figure adapted from Weisman and Klemp (1982). ©American Meteorological Society. Used with permission.

https://doi.org/10.1017/9781009485654.012 Published online by Cambridge University Press

horizontal wind direction turns with height (Markowski and Richardson, 2010). This is also referred to as turning wind shear. As shown in Figure 11.3, simulations with $25\,\mathrm{m\,s^{-1}}$ vertical wind shear or more show no drop in maximum updraft speed below $15\,\mathrm{m\,s^{-1}}$.

11.2.1 Vorticity

The self-organization of convective storms is related to the generation of relative vertical vorticity inside a storm. Relative vorticity is a quantity that is measuring the spin of a local portion of a fluid, in our case air. In multicells and supercells, whose horizontal extent is several tens of kilometers (Table 11.1) and for which the Rossby number *Ro* (eq. 4.49) is much greater than one, we can neglect the planetary vorticity and focus only on the *relative vorticity*. In the following, we refer to relative vorticity whenever using the term vorticity, unless otherwise stated. Regions with high values of vertical vorticity are often observed in clouds belonging to MCSs or supercells. A strong vertical vorticity maximum inside the cloud acts to maintain the updrafts. In order to understand this reinforcement, we now discuss the sources of vorticity in convective cloud systems.

The vorticity vector can be defined at every point of the domain as the curl of the three-dimensional velocity field:

$$\vec{\omega} = \nabla \times \vec{v}. \tag{11.1}$$

Hence, the three vorticity components along the *x*-, *y*-, and *z*- directions are given by

$$\eta = \frac{\partial w}{\partial y} - \frac{\partial v}{\partial z}, \tag{11.2}$$

$$\xi = \frac{\partial u}{\partial z} - \frac{\partial w}{\partial x}, \tag{11.3}$$

$$\zeta = \frac{\partial v}{\partial x} - \frac{\partial u}{\partial y}, \tag{11.4}$$

where u, v, and w denote the *x*-, *y*-, and *z*- components of the velocity vector $\vec{v}$, respectively. Equations (11.2)–(11.4) show that vorticity is generated by wind shear, in the horizontal and vertical winds.

Horizontal vorticity is important for phenomena occurring on the mesoscale, for which $Ro > 1$ (eq. 4.49), such as ordinary, multicell, and supercell convective storms, which are characterized by horizontal extents of $\sim 10 - 100$ km (Figure 1.24 and Table 11.1)

In these cloud systems, the height of the troposphere can be on the same order of magnitude as their horizontal extents. The primary source of horizontal vorticity on the mesoscale is the vertical wind shear $(\partial u/\partial z, \partial v/\partial z)$, as shown in Figure 11.4a. In the presence of updrafts, this horizontal vorticity can then be converted into vertical vorticity.

To better understand the sources of relative vorticity (horizontal and vertical) in mesoscale systems, we start from the equations describing the temporal evolution of relative vorticity for a fluid parcel in an incompressible flow:

https://doi.org/10.1017/9781009485654.012 Published online by Cambridge University Press

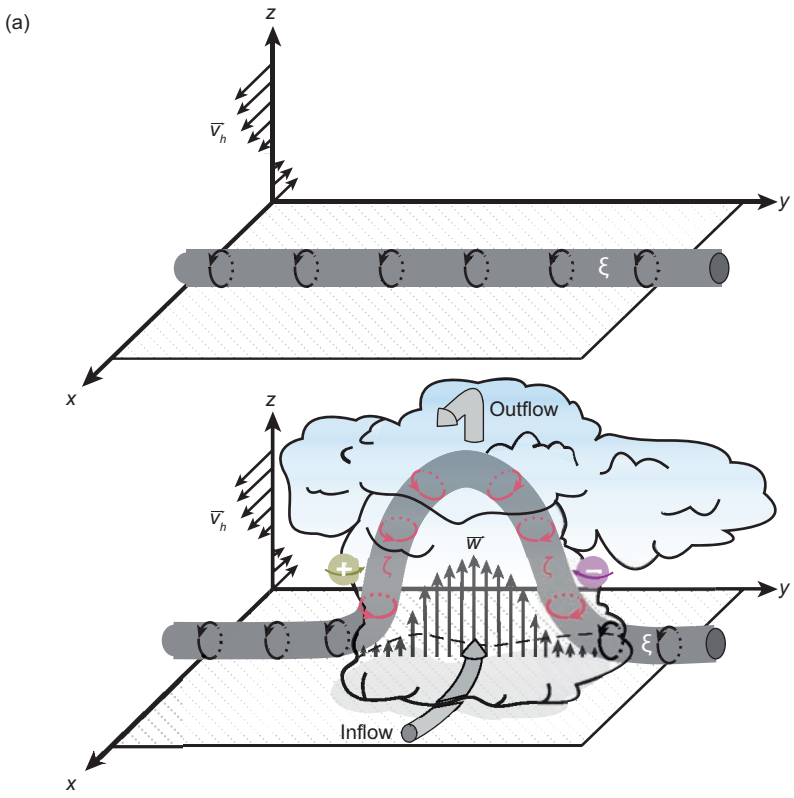


Figure 11.4 Conversion of horizontal vorticity in the y-direction ξ into vertical vorticity ζ in a convective storm in the presence of vertical wind shear $\partial\vec{v}_h/\partial z = (\partial u/\partial z, 0)$ indicated by the black arrows along the z-axis. (a) The creation of ξ (illustrated by the gray vorticity tube) by $\partial u/\partial z$. (b) The creation of ζ by the superposition of an updraft of a convective cloud on a horizontal vorticity tube. "+" signs denote cyclonic ζ and "–" signs anticyclonic ζ on the Northern Hemisphere. The thick gray arrows show the in- and outflow, and the thin vertical black arrows denote the updrafts. The circular arrows around the gray tubes indicate the vorticity. Note how the tilting of ξ by the updraft mainly causes the generation of ζ at mid levels, while the production of ζ at the ground is negligible. Figure adapted from Klemp (1987) and based on Rotunno (1981). ©American Meteorological Society. Used with permission.

$$\frac{d\eta}{dt} = \frac{\partial F_B}{\partial y} + \eta\frac{\partial u}{\partial x} + \xi\frac{\partial u}{\partial y} + \zeta\frac{\partial u}{\partial z} + F_\eta \tag{11.5}$$

$$\frac{d\xi}{dt} = -\frac{\partial F_B}{\partial x} + \eta\frac{\partial v}{\partial x} + \xi\frac{\partial v}{\partial y} + \zeta\frac{\partial v}{\partial z} + F_\xi \tag{11.6}$$

$$\frac{d\zeta}{dt} = \underbrace{\zeta\frac{\partial w}{\partial z}}_{\text{stretching}} + \underbrace{\xi\frac{\partial w}{\partial y} + \eta\frac{\partial w}{\partial x}}_{\text{tilting}} + \underbrace{F_\zeta}_{\text{mixing}}. \tag{11.7}$$

https://doi.org/10.1017/9781009485654.012 Published online by Cambridge University Press

In eqs. (11.5) and (11.6), F_B denotes the buoyancy force. Its horizontal gradient creates horizontal vorticity. Equation (11.7) is known as the relative vorticity equation in the z-direction. The first term on the right-hand side of eq. (11.7) is referred to as the stretching term, which is positive if the vertical velocity increases with height.

ζ can be obtained from the horizontal convergence of the horizontal wind, that is, the continuity equation for the case of the incompressible flow (ρ_a = constant). The assumption of an incompressible flow is often applied in the atmosphere because it eliminates changes in air density with time and simplifies the continuity equation to:

$$\nabla \cdot \vec{v} = \frac{\partial u}{\partial x} + \frac{\partial v}{\partial y} + \frac{\partial w}{\partial z} = 0. \tag{11.8}$$

A direct consequence of the continuity equation is that horizontal convergence or divergence initiates vertical motion. Neglecting both the tilting and mixing terms in eq. (11.7) and inserting eq. (11.8) into eq. (11.7), we obtain

$$\frac{d\zeta}{dt} = -\zeta \left(\frac{\partial u}{\partial x} + \frac{\partial v}{\partial y} \right). \tag{11.9}$$

This equation implies that convergence $(\partial u/\partial x + \partial v/\partial y) < 0$ in the presence of some vertical vorticity ζ further increases the vertical vorticity, that is, the fluid spins faster. This stretching effect can be understood using the principle of *angular momentum m* conservation:

$$m = r v_t + \frac{1}{2} f r^2, \tag{11.10}$$

where v_t is the tangential wind speed in cylindrical coordinates and f denotes the Coriolis parameter. For a solid body rotation, as occurring, for example, in the eye of a TC or in a tornado, v_t is related to the angular velocity ω as follows:

$$v_t = \omega r. \tag{11.11}$$

An example of angular momentum conservation is vertical stretching of a column of air (or vortex tube within the updraft), which reduces its radius and causes the air column to rotate faster.

The tilting terms in eq. (11.7) describe the generation of vertical vorticity ζ by the tilting of horizontal vortex tubes (i.e., horizontal vorticity, eqs. 11.5 and 11.6), as illustrated in Figure 11.4b. When the updraft of the convective cloud is superimposed on the vortex tube, the tube is deformed upward along the updraft gradient ($\partial w/\partial x, \partial w/\partial y \neq 0$). In that way, vorticity develops around the vertical axis, that is, horizontal vorticity is converted into vertical vorticity ζ. After the creation of some initial ζ, the stretching term in eq. (11.7) becomes important in the updraft region, which is characterized by convergence and ascending motions. Note that Figure 11.4b illustrates the simple case of conversion of horizontal vorticity purely in the y-direction ξ into vertical vorticity ζ. Certainly, the same holds true for the conversion of horizontal vorticity in the x-direction η into vertical vorticity, or horizontal vorticity that has both non-zero η and ξ values. The mixing term in eq. (11.7) denotes friction. Friction is usually small, unless close to the Earth surface, and therefore neglected.

In Figure 11.5b, we illustrate how downdrafts and buoyancy generate horizontal vorticity. In the mature stage of the convective storm, precipitation creates downdrafts, which warm the

https://doi.org/10.1017/9781009485654.012 Published online by Cambridge University Press

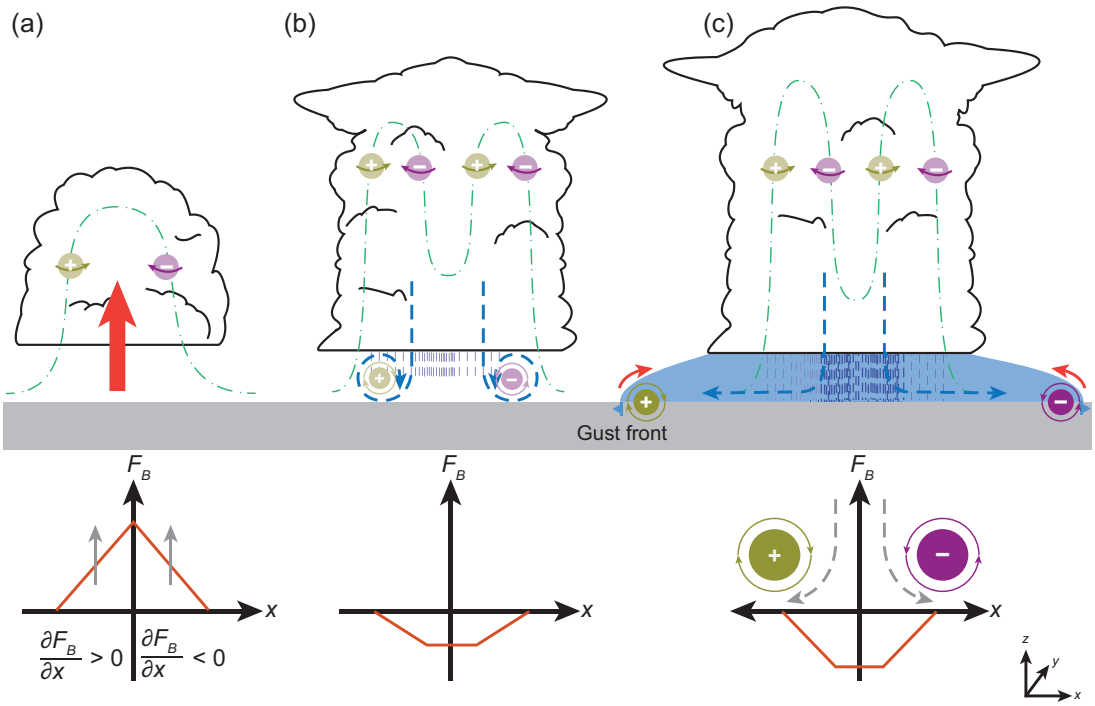


Figure 11.5 The generation of horizontal vorticity ξ in the y-direction by a gradient in the horizontal buoyancy force F_B (orange solid line) in the x-direction in a single cell convective storm: (a) cumulus stage with positive F_B; (b), (c), mature stages with negative F_B at the surface creating a pair of vortices of different signs and intensities (colored circles, the darker circles correspond to greater intensity) according to eq. (11.12). The blue color denotes the cold air outflow that is separated from the warmer air by the gust fronts.

air by adiabatic compression. Near the surface, the downward motion is slowed, and cooling by evaporation, sublimation, and/or melting of the hydrometeors dominates over the warming by adiabatic compression, leading to a negative temperature anomaly. This negative temperature anomaly at the surface induces a horizontal buoyancy gradient $\frac{\partial F_B}{\partial x}$, as illustrated in Figure 11.5b,c: This horizontal gradient in F_B creates horizontal vorticity ξ in the form of two vortices that rotate clockwise (positive ξ to the left/west; green circle, also called *cyclonic vorticity*) and anticlockwise (negative ξ to the right/east; purple circle, also called *anticyclonic vorticity*). Mathematically, this is described by the ξ-component of the vorticity equation (eq. 11.6), which, in the absence of the stretching and tilting terms and friction, is given by:

$$\frac{d\xi}{dt} = \frac{\partial \xi}{\partial t} + u\frac{\partial \xi}{\partial x} + w\frac{\partial \xi}{\partial z} = -\frac{\partial F_B}{\partial x}. \tag{11.12}$$

This buoyancy-generated horizontal vorticity adds to the horizontal vorticity ξ generated by the environmental vertical wind shear, as illustrated in Figure 11.6a. Careful investigation of Figure 11.6a reveals that the ξ generated by the horizontal wind vector relative to the storm movement ($\frac{\partial \vec{v}_{rel}}{\partial z}$) has the same sign as the ξ generated by the buoyancy anomaly at the surface to the west (left) of the storm. To the east (right) of the storm, the buoyancy-generated ξ has

https://doi.org/10.1017/9781009485654.012 Published online by Cambridge University Press

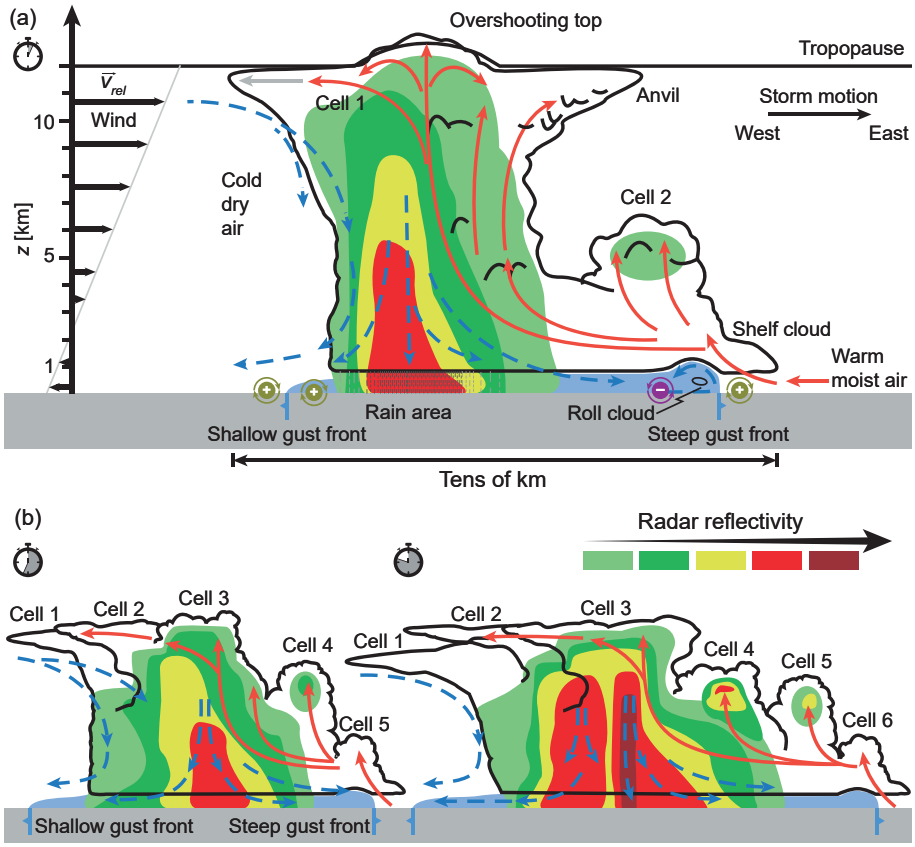


Figure 11.6 (a) Schematic view of the motion of the warm moist air (solid red arrows) and the cold dry air (broken blue arrows) in a multicell storm. The storm is moving from left to right. The wind vectors relative to the storm movement $\vec{v}_{rel}$ are indicated on the y-axis. (b) Temporal evolution of a multicell convective storm, along with up- and downdrafts. Also shown are approximate boundaries of different radar reflectivities as well as the cold air outflow that is separated from the warmer air by the gust fronts (in blue color). Figure panels a and b are after Ahrens (2019) and Doswell (1985).

the opposite sign of the environmental wind-generated ξ, which causes convergence of air at the surface gust front and strong uplift. The horizontal vorticity generated behind the gust front can sometimes be visible as a "roll" cloud behind the gust front or sometimes as a shelf cloud ahead and above the gust front, as shown in Figure 11.6a.

The uplift of air at the gust front converts ξ into ζ via the tilting terms in eq. (11.7), which can be further strengthened by buoyancy, that is, an updraft, and the stretching term in eq. (11.7). This extra vorticity generation from the gust front associated with the forward flank downdraft is indicated by the blue arrow in Figure 11.7. It intensifies the existing convective storms if the gust front remains underneath the cloud systems, as it does in multi- and supercell convective storms (Figure 11.6), because it adds to the positive ζ once it is swept into the updraft.

Overall, the development of vorticity in strong convective storms (multi- and supercells) can be summarized as follows: (i) Strong convective storms usually occur in areas with moderate to

https://doi.org/10.1017/9781009485654.012 Published online by Cambridge University Press

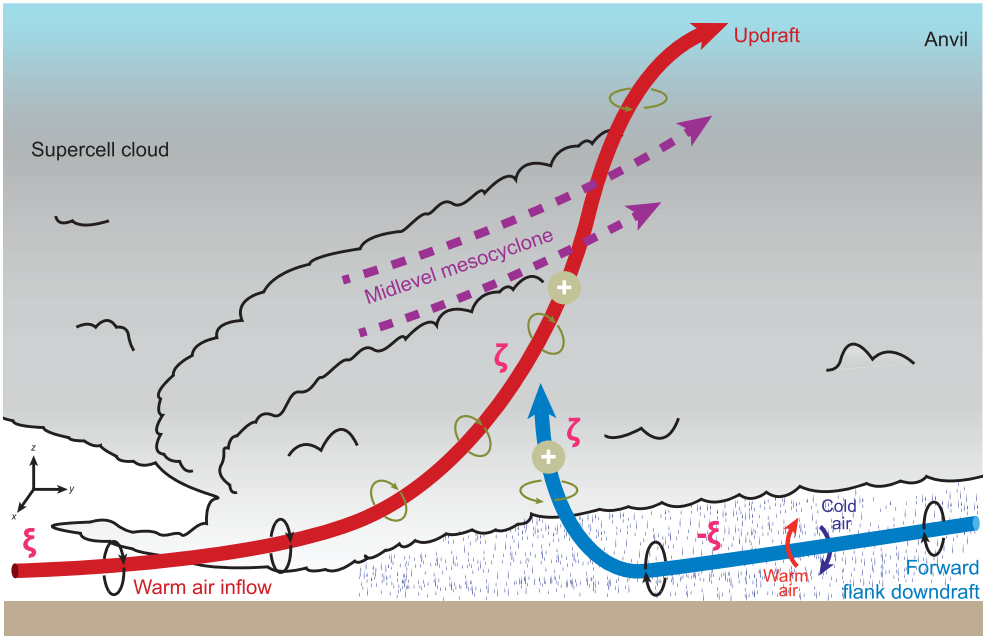


Figure 11.7 Schematic illustrating the three main sources of rotation in a supercell (Houze, 2014): (i) The updraft tilts positive horizontal vorticity ξ in the inflow in the warm section of the supercell into the cloud (see Figure 11.4b), generating vertical vorticity ζ. (ii) This vertical vorticity can be intensified by the stretching term (vertical part of the red arrow; eq. 11.7). (iii) The forward flank downdraft generates negative horizontal vorticity ($-\xi$) with cool air behind the gust front and warm air ahead of it (eq. 11.5), which is tilted into positive vertical vorticity (ζ) near the surface under the rotating updraft. The loops show the vorticity vector at various locations along the updraft and downdraft. The cloud is shaded and precipitation is hatched. The rear flank downdraft is not visible in this figure.

strong vertical wind shear, which implies the generation of horizontal vorticity (eqs. 11.5, 11.6 and Figure 11.4a); (ii) Tilting of horizontal vorticity by an updraft creates vertical vorticity, which can be intensified by stretching (eq. 11.7 and red arrow in Figure 11.7); (iii) Precipitation consumes latent heat and generates a horizontal gradient in F_B and horizontal vorticity (eq. 11.12), thus continuing with (ii).

This positive feedback loop can generate very high values of ζ inside a convective storm (Table 11.1), which in turn reinforces the up- and downdrafts that cause the longevity of multi- and supercell storms. In the case of supercells, this feedback loop is responsible for their characteristic mesocyclones (Section 11.2.3).

11.2.2 Multicell Storms

Multicell storms are larger (several tens of kilometers in horizontal dimensions), last longer, have higher CAPE values, and occur less frequently than ordinary storms (Markowski and Richardson, 2010, Table 11.1). The name arises because a multicell storm consists of several convective cells, each in a different stage of development.

https://doi.org/10.1017/9781009485654.012 Published online by Cambridge University Press

A schematic of the air motions and other features associated with an intense multicell storm is shown in Figure 11.6. The individual cells can be characterized into an early, a mature, or a dissipating stage (Figure 11.1). In Figure 11.6a, a small second cell (in the early cumulus stage) is appearing ahead (i.e., downwind in the direction of storm motion) of the initial cell (now in the mature stage). The inflowing warm moist air in both the initial and second cells is shown by the curved red arrows. Like the ordinary convective storm in Figure 11.1, a multicell storm also has an overshooting top that protrudes into the stratosphere with a pronounced anvil, under which mammatus clouds (Figure 1.11c) often form.

In contrast to an ordinary convective storm, the updraft is considerably tilted because of the moderate vertical wind shear associated with multicell storms, as indicated by the horizontal black arrows in Figure 11.6a. Underneath the multicell storm, the cold air from the downdraft spreads out horizontally. However, the outflow of multicell storms encounters more resistance due to the stronger low-level inflow relative to the storm motion as compared to an ordinary cell, and thus cannot horizontally advance as far away from the downdraft's splash point.

Thus, in multicells, the gust front moves with the storm (Figure 11.6) and the cold and dense air behind the gust front helps to lift the warm moist air and allows new cells to repeatedly form ahead (downwind) of the main updraft. We note that the slope of the gust fronts depends on the vertical wind shear, as illustrated in Figure 11.6a: The slope of the gust front forming on the east underneath the second convective cell is steeper compared to the one forming underneath the initial convective cell on the west. This is because the wind relative to the storm movement blows from east to west near the surface in our example, causing resistance to the advancing gust front. In this first stage, the anvil spreads out symmetrically to both sides of the mature convective cell (cell 1). The anvil does not extend further to the downwind side because of the new air that is continuously lifted up in younger cells (cell 2), in the direction of the storm motion.

If the lifted air is sufficiently moist, a shelf cloud (Figure 11.6a) forms in the lifted inflowing warm air ahead of the gust front. Shelf clouds are a visual manifestation that the approaching storm will be severe. This self-perpetuating triggering of new convective cells along the gust front is characteristic of multicell storms and the reason for their longevity: While each individual cell only lasts for approximately 30–60 min, the multicellular convection can last for hours. The mature cell in multicellular storms can sometimes rotate and form a mesocyclone, although a mesocyclone is more typical in supercells (Cotton et al., 2011).

The temporal evolution of a multicellular storm with new cells forming along the gust front is illustrated in Figure 11.6b. Over time, new convective cells repeatedly form ahead of the main updraft region. By contrast, behind the main updraft, the vertical air motions weaken, and the cells reach their dissipating stage, taking on stratiform character. Because of the weaker updrafts in the anvils, the ice particles can sediment against the updrafts and cause the entire anvil to lower itself with time. The lifetime of the anvil depends on the microphysical processes within the anvil cloud. While large ice crystals sediment from the anvil within a few hours and thus cause the anvil to disappear, depositional growth and potentially nucleation of new ice crystals can contribute to anvil persistence (Jensen et al., 2018). This leads to anvil cirrus lifetimes of 3–5 h in the extratropics, while in the tropics anvils can persist for up to 12 h (Mace et al., 2006).

https://doi.org/10.1017/9781009485654.012 Published online by Cambridge University Press

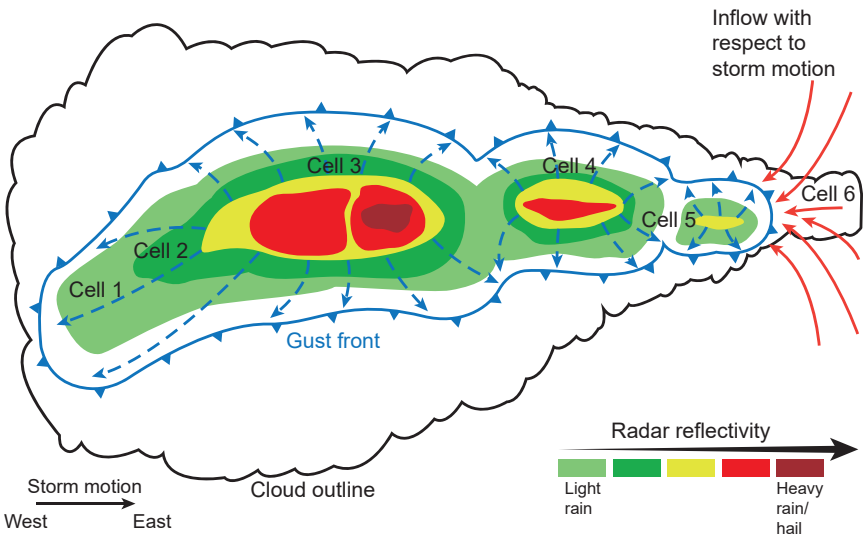


Figure 11.8 Schematic top view of a precipitation radar image associated with a multicell storm, as depicted in Figure 11.6.

The outline of the large cirriform anvil of a multicell storm is indicated in Figure 11.8. The anvil is mostly invisible in the precipitation radar image, because the ice crystals are too small to be seen by the precipitation radar (Figure 10.5). Typical for a multicell storm is that its horizontal extent is largest in the direction of storm motion.

11.2.3 Supercell Storms

Supercell storms are more violent and destructive than multicell convective storms. They occur less frequently than multicell storms because they need an even stronger vertical wind shear in the lowest 6 km than multicell storms (Table 11.1). There are two ingredients that promote the longevity of supercells: (i) the gust front remaining within the system (as in multicells) and (ii) the turning wind shear (vs. unidirectional wind shear in multicells) causing the updraft and downdrafts to be spatially displaced.

The vertical wind shear generally turns anticyclonically with altitude when supercell storms form in the United States (Klemp, 1987; Markowski and Richardson, 2010; Bluestein, 2013). A typical situation in which low-level warm and moist air with an anticyclonic-turning wind shear can be found is when low-level air from the south originates over the Gulf of Mexico while the air at mid levels comes from the west or north. Such a setting causes a large contrast between warm and moist air masses near the surface and cold and dry air masses aloft. It is the reason why supercell storms and tornadoes occur frequently in the United States and why the so-called *Tornado Alley*[4], located in the midwest of the United States is a tornado hot-spot (Brooks et al., 2003).

[4] https://glossary.ametsoc.org/wiki/Tornado_alley

https://doi.org/10.1017/9781009485654.012 Published online by Cambridge University Press

Next to this dynamical prerequisite, suitable thermodynamic conditions need to be present for the formation of supercell storms, namely, ample low-level moisture and a sufficiently high CAPE value, that is, adequate instability for vigorous convection to occur (Table 11.1).

Supercell storms have a horizontal extent comparable with multicell convective storms but consist of a single giant updraft-downdraft pair with strong vertical velocities of 10–40 $m\,s^{-1}$ (Figure 11.3). In some extreme cases, the top of the supercell storm may extend into the stratosphere, and the width of the storm may exceed 50 km (Table 11 and Markowski et al., 2018).

Supercell storms are often isolated from other convective storms, but merging supercells also occur (Flournoy et al., 2022). Supercells are characterized by a mesocyclone[5] (Figure 11.9). A mesocyclone is a deep updraft that is persistently rotating cyclonically around a vertical axis in the supercell that is moving to the right (right mover (RM)). The few left-moving supercells produce a mesoanticyclone, which is an anticyclonically moving updraft (Davies-Jones, 2015). The vorticity associated with a mesocyclone is often on the order of $10^{-2}\,s^{-1}$ or greater (Markowski et al., 2008). It is worthwhile noting that mesocyclones do not simply describe any cyclone on the mesoscale, but specifically refer to cyclones in supercells and sometimes multicells (Cotton et al., 2011). Severe convective storms, such as supercells and MCSs, typically occur over land in the tropics and in midlatitudes (Zipser et al., 2006), and can be found in the warm sector of a low-pressure system generally propagating in a northeasterly direction in the Northern Hemisphere (Davies-Jones, 2015). Supercell storms often produce hail and can transition into tornado-breeding supercells as shown in Figure 11.9, but can also occur without the formation of a tornado (Trapp et al., 2005b). Similarly, tornadoes can also form

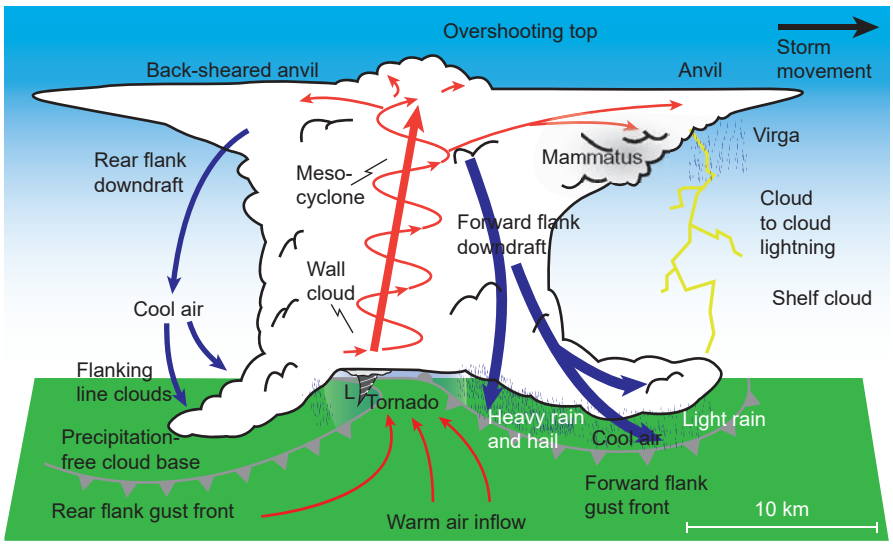


Figure 11.9 Schematic of the main features, including the updraft, downdrafts, and surface air flow, associated with a tornado-breeding supercell convective storm in the Northern Hemisphere.

[5] https://glossary.ametsoc.org/wiki/Mesocyclone

https://doi.org/10.1017/9781009485654.012 Published online by Cambridge University Press

without a mesocyclone. These are called *non-supercell tornadoes*[6] (Roberts and Wilson, 1995) or, depending on their location, either *landspouts* or *waterspouts*[7]. Non-supercell tornadoes are typically smaller and weaker than supercell tornadoes.

As in a multicell storm, the updraft in a supercell storm is tilted because of the vertical wind shear, and the areas of precipitation are separated from the updraft. A supercell storm is characterized by two marked downdrafts, the *forward flank downdraft* and the *rear flank downdraft*, upstream and downstream of the storm, respectively. The forward flank downdraft is the larger one and is the one that is referred to when describing the supercell as a giant updraft–downdraft cell. Consequently, a supercell also has two gust fronts, one ahead of the storm, associated with the forward flank downdraft, and one behind the storm, associated with the rear flank downdraft. The first light rain forms behind the forward flank gust front, followed by heavy rain and hail as the center of the forward flank downdraft approaches. Ahead of the rear flank gust front a line of cumulus clouds forms as surface air is lifted into the storm along the rear flank gust front, forming the flanking line of the supercell storm, where precipitation is mostly absent. In fact, most hydrometeors in the updrafts are advected downwind into the northeastern part of the supercell, that is, into the forward flank, due to the turning vertical wind shear. This results in a characteristic asymmetry in the radar echos of supercells, with high overhanging radar-reflectivity in the forward flank region and low radar-reflectivity in the rear flank region (Figure 11.10a).

By contrast, the rear flank downdraft is forced downward by mid-level environmental winds and warms by adiabatic compression. There are currently two hypotheses for this forced air movement: (i) either it is caused by pressure perturbations ($\tilde{p}/p_{env}$) with a positive pressure anomaly in upper levels and a negative pressure anomaly in lower levels. Alternatively, (ii) it is caused by entrainment of dry environmental air in which hydrometeors evaporate/sublimate and reduce buoyancy. The hydrometeor weight q_H reduces buoyancy as follows:

$$F_B = -g\frac{\tilde{\rho}}{\rho_{a,env}} \approx g\left(\frac{\tilde{T}}{T_{env}} - \frac{\tilde{p}}{p_{env}} + 0.61\tilde{q}_v - q_H\right), \tag{11.13}$$

where the second term on the right side denotes the pressure perturbation that can give rise to buoyancy. The third term arises because humid air is less dense than dry air. In a supercell, this cooling can decrease the surface temperature by 2–10 K (Markowski and Richardson, 2010).

If the subsiding air is dry, the rear flank downdraft is characterized by a slot of cloud-free air and a rain-free base where the temperature increases dry adiabatically. If the subsiding air contains hydrometeors, the downward motion in the rear flank downdraft is partly driven by their loading and partly by latent heat consumption due to their evaporation/melting. Both the rear flank downdraft and the forward flank downdraft are thought to be important for producing (spawning) tornadoes, as will be discussed in Section 11.2.5.

Figure 11.9 shows that the inflow into the supercell at the surface is almost perpendicular to the main wind direction, with which the storm moves. The convergence of the warm, moist inflowing air with the cooler air from the supercell downdrafts leads to the formation of cold

[6] https://glossary.ametsoc.org/wiki/Nonsupercell_tornado
[7] https://glossary.ametsoc.org/wiki/Waterspout

https://doi.org/10.1017/9781009485654.012 Published online by Cambridge University Press

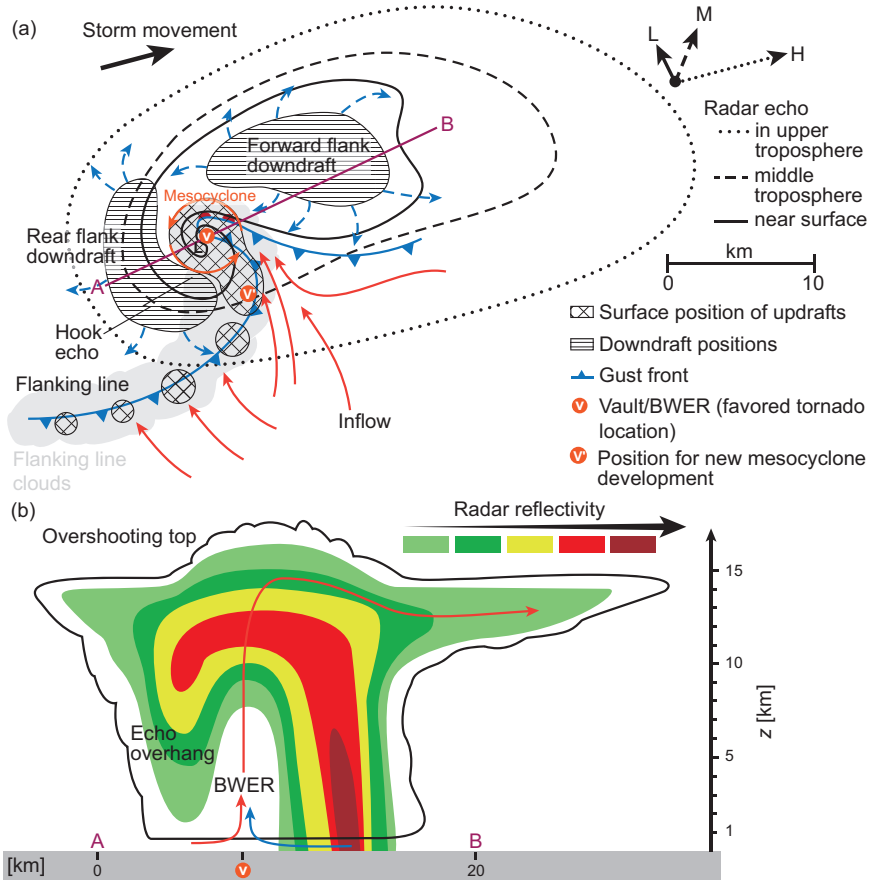


Figure 11.10 Supercell storm: (a) Schematic diagram showing horizontal sections of the radar echoes at three different height levels of a supercell storm. Environmental winds relative to the storm at low, medium, and high levels of the troposphere are represented by the three vectors low (L), middle (M), and high (H). Near surface locations of the forward flank downdraft and the rear flank downdraft are shown by the striped patterns, whereas updfraft regions are checkered. The most likely location for a cyclonic tornado is at the apex of the gust front and is represented by a "V" (vault or bounded weak echo region (BWER)). The location marked with a V' at the bulge of the gust front indicates the region where a new mesocyclone may develop. The location marked with L denotes the low-pressure center. (b) Vertical cross section from points A to B through the supercell storm shown in panel (a), showing the approximate radar reflectivity structure of a supercell storm. Also illustrated are the relationship between the overshooting top, BWER, and radar hook echo. Panel (a) is adapted from Davies-Jones (2015) and is based on the original drawing of Lemon and Doswell (1979). Published (1979) by the American Meteorological Society.

https://doi.org/10.1017/9781009485654.012 Published online by Cambridge University Press

and warm fronts at the surface. Unlike the surface cold and warm fronts in an extratropical low-pressure system, the cool air in the supercell approaches from both behind and ahead of the warm air. Since the horizontal wind turns anticyclonically with altitude, a good portion of the outflow at upper levels is almost parallel to the main wind direction (storm motion), as illustrated in Figure 11.10a.

Supercell storms are characterized by an extensive overhanging radar echo ahead of the storm, which slopes downward to the surface toward its rear flank, as seen by comparing the radar echo boundaries at different altitudes in Figure 11.10a. In between the forward flank downdraft and the rear flank downdraft, there is the updraft region of the supercell associated with low radar reflectivity, called the *vault* or *bounded weak echo region (BWER)*. The BWER can best be observed in a vertical cross-section of a supercell storm, and can extend vertically up to 10 km, as shown in Figure 11.10b. The BWER marks a region where the updraft is too strong for hydrometeors to fall against it. It is depicted as V for "vault" in Figure 11.10a and is located at the bulge (vault) of the near-surface radar echo (Browning, 1964). At low altitudes, the BWER might not be bounded underneath the rear flank downdraft (Figure 11.10b). The BWER is capped at higher altitudes, where updrafts weaken and hydrometeors become large enough to fall against the updrafts. Radar echos extend downward at both sides of the updraft region, with the largest echoes in the forward flank downdraft.

In summary, unless the environmental winds have a turning wind shear, the updraft and downdraft in a convective storm cannot become intertwined and neither a mesocyclone nor a tornado can form from the supercell.

11.2.4 Unidirectional Versus Turning Wind Shear

In an environment with vertical wind shear, convective storms propagate approximately $60°-90°$ relative to the main synoptic flow. In the example in Figure 11.11, the main flow is southwesterly and the vertical wind shear of the environmental wind is shown in the form of a *hodograph* (Figure 11.11a). In a hodograph, the u-component of the wind speed (west-to-east) is shown on the x-axis and the v-component of the wind speed (south-to-north) is shown on the y-axis. Moreover, the numbers on the straight gray and curved blue lines indicate the respective altitudes. We will make use of the hodograph when discussing the two possibilities how supercells propagate, depending on the nature of the wind shear (unidirectional vs. turning), shown in Figure 11.11.

Let us start with unidirectional (non-turning) vertical wind shear, where only the wind speed increases with height but one wind component remains constant (gray line in hodograph). In this case, $v = 12\,\mathrm{m\,s^{-1}}$ from the surface until a height of 7.5 km. u changes from $-10\,\mathrm{m\,s^{-1}}$ (easterly wind) at the surface to $> 50\,\mathrm{m\,s^{-1}}$ (westerly wind) at 7.5 km. In such a scenario, the convective storm develops symmetrically, as shown by the storm track in Figure 11.11b. After 40 min, the updraft has a maximum value of $9\,\mathrm{m\,s^{-1}}$ in the center of the convective storm (left panel in Figure 11.11b). This is the region where the hydrometeors grow largest in size and start to fall against the updraft, leading to a downdraft and a gust front. The gust front does not propagate symmetrically away from the region of heaviest precipitation but is a superposition of the environmental wind and the storm-scale motions. Owing to the easterly inflow at the

https://doi.org/10.1017/9781009485654.012 Published online by Cambridge University Press

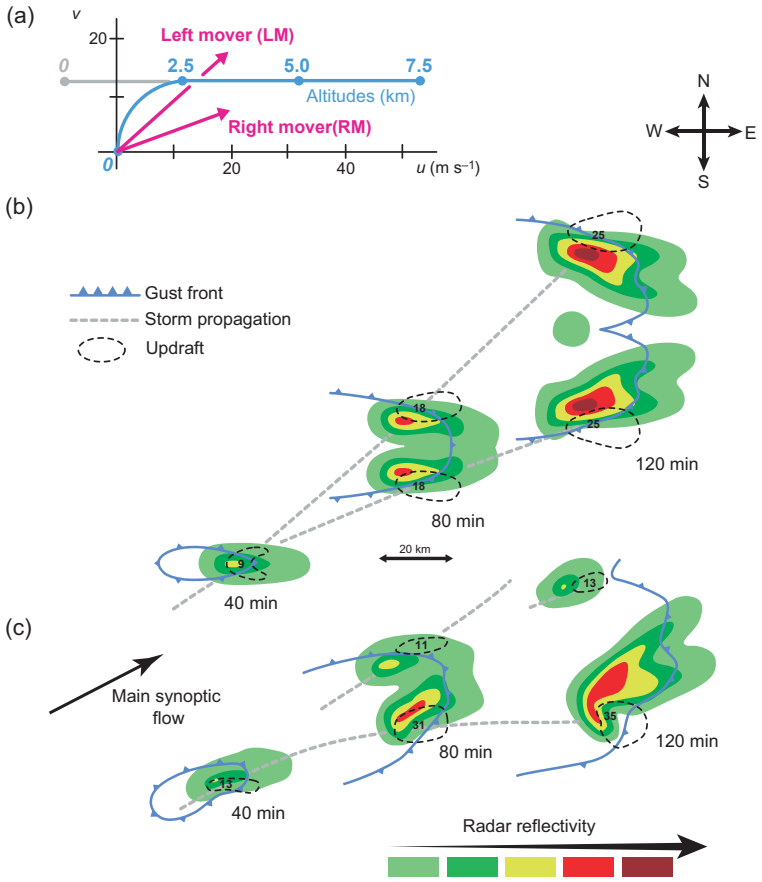


Figure 11.11 Propagation of convective storms in an environment with unidirectional vertical wind shear (b) and turning environmental wind shear (c). The color shading indicates radar reflectivity (color bar) as seen from above. The blue lines with triangles denote the gust front. The black dotted lines denote the location of the updrafts, and the values inside them denote the maximal updraft speed in $\mathrm{m\,s^{-1}}$. The gray dashed lines denote the propagation of the individual cells. The environmental wind shear is indicated in the form of a hodograph in the insert on the upper left (a). It shows the wind direction and speed at 0 km, 2.5 km, 5 km, and 7.5 km altitude for unidirectional shear (gray line) and turning shear (blue line). Figure modified from Markowski and Richardson (2010) and based on Klemp (1987). Used with permission.

surface, the gust front remains within the system on the eastern flank. Here it pushes the inflow and thus the updraft (black dashed lines) to both sides (northeast and southeast) of the storm.

After 80 min, this results in a so-called *storm-splitting*, as shown in the middle panel of Figure 11.11b. The storm-splitting is completed after 120 min with a radar-free region inbetween both cells. The updrafts on the sides of the two cells increased from 18 $\mathrm{m\,s^{-1}}$ after 80 min to 25 $\mathrm{m\,s^{-1}}$

https://doi.org/10.1017/9781009485654.012 Published online by Cambridge University Press

after 120 min. In such a setting, both storm cells have identical strength and they are lacking the supercell structure with the characteristic vault or BWER.

Let us now consider a scenario with turning environmental vertical wind shear as depicted in the blue line in the hodograph (Figure 11.11a). Here, the wind speed at the surface is 0 in both x and y direction and increases to $u = v = 12\,\mathrm{m\,s^{-1}}$ at 2.5 km in a clockwise, anticyclonic rotating manner. The anticyclonic rotation results because first v is increasing and afterwards u as well. Above this altitude, only the u-component of the wind strengthens, identical to the case with unidirectional shear.

The influence of turning shear is already visible after 40 min in Figure 11.11c: the updraft is stronger on the eastern side of the storm, and the gust front shows the first indications of a bent structure. After 80 min storm splitting occurs, but the updraft in the RM is significantly stronger with a vertical velocity of $31\,\mathrm{m\,s^{-1}}$ compared to the left mover (LM) with an updraft of only $11\,\mathrm{m\,s^{-1}}$. The reason for this is that the turning vertical wind shear induces pressure anomalies such that there is a high-pressure anomaly at the surface of the RM and a low-pressure anomaly in its upper levels (Klemp, 1987). These pressure anomalies enhance the updraft. The pressure anomalies are of opposite sign for the LM and work against the updraft. After 120 min, the supercell is fully developed with a $35\,\mathrm{m\,s^{-1}}$ updraft, a visible hook-shaped radar echo, and a BWER (Markowski and Richardson, 2010). This set-up is very typical for supercells over the United States. In fact, Klemp (1987) showed that 140 out of 143 investigated supercell storms over the united states are RMs. Note that while supercells form in an environment of anticyclonic environmental shear, the rotation inside the supercell is cyclonic. This is a result of the gust front remaining in the system and creating horizontal vorticity, which is advected back into the supercell as visualized by the blue arrows in Fig. 11.7. Upon coming in close proximity of the updraft, the horizontal vorticity is tilted and strengthens the existing updraft.

11.2.5 Tornadoes

Tornado Characteristics

A tornado is generally defined as a rapidly rotating column of air in contact with the ground, underneath a cumulus cloud. Often it is visible as a funnel cloud, but it can be obscured by heavy precipitation. A funnel cloud is a cone-shaped or needle-like protuberance hanging downwards from the cloud base, which may or may not be in contact with the ground[8]. A tornado is associated with a strong local pressure minimum and very high wind speeds in both the vertical and horizontal directions. The median tornado diameter is 250–500 m with 10–15 % of the cases exceeding 1 km (Wurman et al., 2021). Most tornadoes rotate cyclonically in the Northern Hemisphere and anti-cyclonically in the Southern Hemisphere. While the tornado is too small to be directly affected by the Coriolis force, it nevertheless tends to spin in the same direction as the warm air inflow curves into the supercell (Figure 11.9), caused by its low pressure in its center. The rotational wind speed of a tornado can be calculated from the cyclostrophic wind balance (eq. 4.58). Tornadoes can reach horizontal wind speeds up to

[8] https://glossary.ametsoc.org/wiki/Funnel_cloud

https://doi.org/10.1017/9781009485654.012 Published online by Cambridge University Press

135 m s^{-1} (490 km h^{-1})[9] and vertical vorticity values of 2 s^{-1} (Tanamachi et al., 2007). Thus, a tornado is the most intense of all circulations on the microscale (Figure 1.24).

Traditionally, the Fujita scale has been used to classify tornadoes into six distinct categories based on the damage caused and the associated wind speeds (Fujita, 1972). Since 2007, the enhanced Fujita scale is more commonly used to describe the intensity of tornadoes (e.g., Potter, 2007).

Tornadogenesis

Tornadoes originate most frequently from supercells, which also spawn the most violent tornadoes (Trapp et al., 2005a). However, non-supercell storms, such as narrow cold-frontal rainbands (Clark and Parker, 2020), QLCSs (Weisman and Davis, 1998; Ashley et al., 2019), and multicells can also spawn tornadoes (Roberts and Wilson, 1995; Markowski and Richardson, 2010). These non-supercell tornadoes occur more frequently in Europe than in the United States because of differences in environmental conditions (Avolio and Miglietta, 2022).

Transition to the tornadic phase occurs relatively suddenly (on the order of 10 min) after a supercell has slowly evolved over several hours (Houze, 2014). During this transition, the low-level rotation (vertical vorticity) increases, which enables the mesocyclone to extend downwards below the cloud and toward the Earth's surface (Burgess and Lemon, 1990; Davies-Jones, 2015). Because the tornado develops between cloud base and the surface, it has been found useful to specify the ingredients for tornadogenesis mainly in the lowest kilometer of the troposphere. Provided that a supercell is present, (i) the vertical wind shear between the surface and 1 km altitude should exceed 10 m s^{-1}. (ii) The LCL is typically lower for supercells with significant tornadoes than those without (Rasmussen and Blanchard, 1998). (iii) A high humidity and a low LCL ensure that the temperature of the downdraft air is not lowered too much by evaporative cooling. This is important for air from the storm's outflow regions, mainly the forward flank downdraft, because the cold air intertwines with the warm inflow air and gets lifted again in the mesocyclone (Figure 11.9). Some CIN is useful because otherwise the atmospheric instability by solar heating at Earth's surface is being removed too early in the day. On the other hand, CIN values cannot be too high, because then no convection occurs.

When a supercell tornado develops, it forms near the edge of the hook-shaped radar echo underneath the mesocyclone. Supercells need strong, storm-scale rotation to develop tornadoes. This rotation near the ground is produced by the vertical environmental wind shear and the rear flank downdraft as follows: First, horizontal vorticity is generated from the strong vertical wind shear close to the surface along the rear flank gust front. At this point in time, vertical vorticity is negligible near the ground (t_0 in Figure 11.12a). Second, this horizontal vorticity is tilted by the updraft, leading to the generation of vertical vorticity, as discussed in Section 11.2.1 (Figure 11.12a). If the tilting of the horizontal vortex is only induced by the updraft, the resulting vertical vorticity mainly develops at mid levels, because the air rises away from the surface as it is tilted by the updraft (t_1 in Figure 11.12a). Third, the downdrafts are a key ingredient for tornadogenesis to produce sufficient vertical vorticity and rotation near

[9] https://wmo.asu.edu/content/tornado-highest-recorded-wind-speed-tornado-doppler-radar

https://doi.org/10.1017/9781009485654.012 Published online by Cambridge University Press

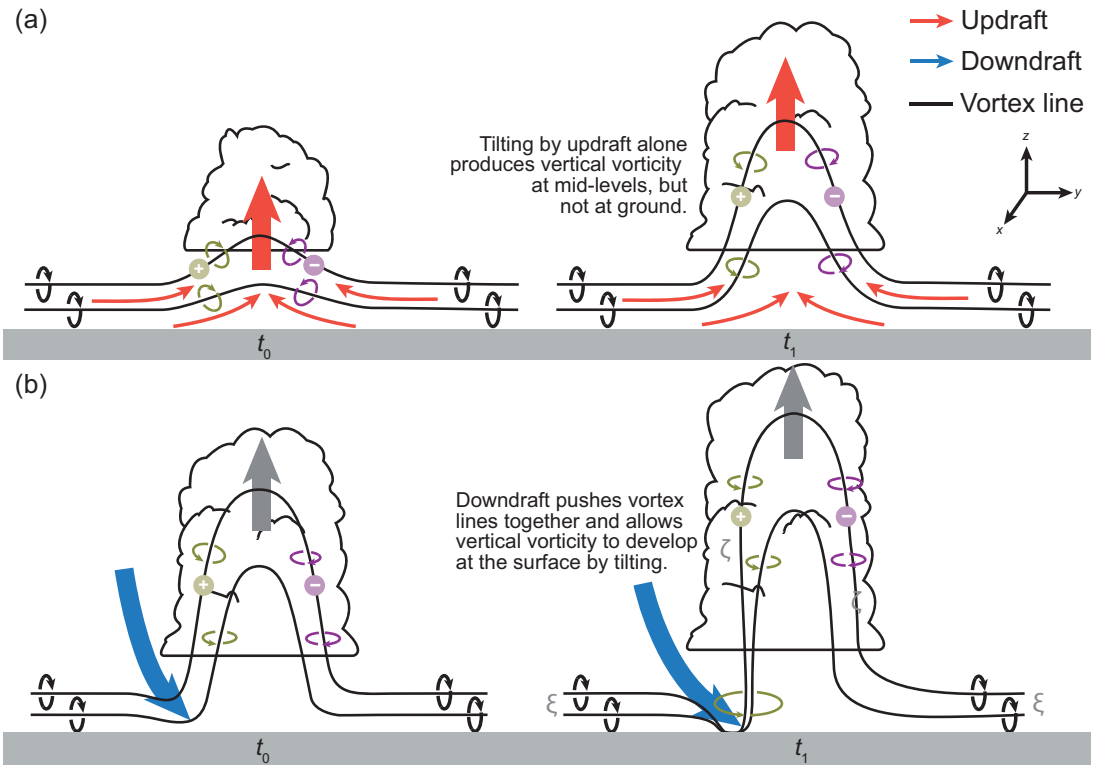


Figure 11.12 Schematic of the generation of vertical vorticity in the (a) absence and (b) presence of the rear flank downdraft. If the tilting of the horizontal vortex lines from environmental wind shear takes place only by an updraft, the air is rising away from the surface as it is tilted, and vertical vorticity is mostly generated at mid levels. A downdraft (in a supercell, the rear flank downdraft) is needed to push the horizontal vortex lines together and to allow tilting to generate vorticity near the surface. Figure adapted from Markowski and Richardson (2010).

Earth's surface: The sinking air in the downdrafts allows vertical vorticity to be transported to Earth's surface and to be kept there (Markowski and Richardson, 2010). The importance of the downdrafts for the generation of near-ground vertical vorticity can be conceived of as vortex lines becoming compressed below the cloud base (t_0 in Figure 11.12b). These converged vorticity lines point upwards all the way from the surface to the cloud when being superimposed by an updraft, as schematically shown in Figure 11.12b (t_1). For the vertical vorticity ζ to become stronger by tilting, the sign of the horizontal vorticity prior to tilting has to be right. This is the case for the horizontal vorticity caused by the forward flank downdraft (e.g., Schueth et al., 2021; Rotunno and Bluestein, 2024). In our case, this is $-\xi$, which upon tilting yields $+\zeta$, see Figure 11.7. As the horizontal vorticity caused by the rear flank downdraft has the wrong sign (being $+\xi$, which upon tilting yields $-\zeta$), the role of the rear flank downdraft is to push the vortex lines closer together as shown in Fig. 11.12b, which marks the initiation of tornadogenesis.

In addition to creating horizontal vorticity, the rear flank gust front causes extra lifting of the inflowing warm buoyant air. The warm rising air and the rear flank downdraft start to spiral

https://doi.org/10.1017/9781009485654.012 Published online by Cambridge University Press

around each other, as can be seen in the hook-shaped radar echo of the rear flank downdraft (Figure 11.10). This spiraling marks the formation of a mesocyclone (Figures 11.7 and 11.9).

Mesocyclones typically have diameters between 3 and 8 km and thus are phenomena occurring at the meso-γ to meso-β scale (Section 10.4). The formation of a mesocyclone distinguishes a supercell storm from a multicell storm and explains why tornadoes in multicell storms are usually much weaker. The *wall cloud* directly underneath the mesocyclone in Figure 11.9 indicates the area of strongest updrafts. Wall clouds form when air masses from the forward flank downdraft region are drawn back into the updraft. These air masses have been cooled by evaporation and hence are characterized by high humidity. Therefore, condensation sets in more readily than in the surrounding air, causing the wall cloud to form at altitudes lower than the rest of the cloud. If the wall cloud and the mesocyclone continue to descend to low levels, a tornado is spawned.

Examples of Tornado Observations and Global Tornado Frequency

An example of two radiosonde profiles from Kansas, USA on May 18, 2013 in an environment where a supercell spawned tornadoes is shown in Figure 11.13. The radiosonde profiles[10] were taken 10 and 4 h prior to the formation of a tornado. At 7:00 local time, the LCL was at 920 hPa, and the humidity in the PBL was well mixed, with a mean specific humidity of 15.9 g kg^{-1}. The boundary layer was confined by a strong inversion of 7 K at its top with a CIN value of 300 J kg^{-1}. Above the inversion, the atmosphere was conditionally unstable. The LFC was located at 640 hPa and the LNB was at 190 hPa, resulting in a CAPE value of 2950 J kg^{-1}. The wind turned anticyclonically from south-southeast at the surface, with warm and humid air originating from the Gulf of Mexico, to southwest at 1 km above the surface (Figure 11.13a).

This sounding is characterized by extreme instability above the capping inversion. Such a sounding is also referred to as a *loaded gun* sounding[11]. In such a case, very rapid convective storm development can be expected if the cap is weakened or the air underneath the cap is sufficiently heated to overcome CIN.

Owing to the solar heating between 7:00 and 13:00 local time, the temperature at the surface (790 m) increased from 20.4 to 32 °C, and T_d decreased from 19.6 to 17 °C. Hence, CIN was reduced to 75 J kg^{-1}, LCL was raised to 730 hPa, LFC to 700 hPa, and CAPE increased to 4400 J kg^{-1} (Figure 11.13b), corresponding to typical CAPE values observed for tornadoes (Table 5.1). The vertical wind shear in the lowest 6 km was 17 m s^{-1}, which, according to Table 11.1, is borderline for supercell development. Thus, only a little extra heating was necessary to overcome CIN and for explosive convective storms to develop. On that day, the extra heating caused the formation of a supercell at 6 pm local time that spawned tornadoes between 7 and 8 pm.

To date, the largest recorded tornado outbreak occurred on April 27, 2011 in the southeastern US with 209 tornadoes[12] (Knupp et al., 2014), four of them being in the most destructive

[10] https://weather.uwyo.edu/upperair/bufrraob.shtml
[11] www.noaa.gov/jetstream/appendix/weather-glossary-ls
[12] https://wmo.asu.edu/content/tornado-largest-tornado-outbreak

https://doi.org/10.1017/9781009485654.012 Published online by Cambridge University Press

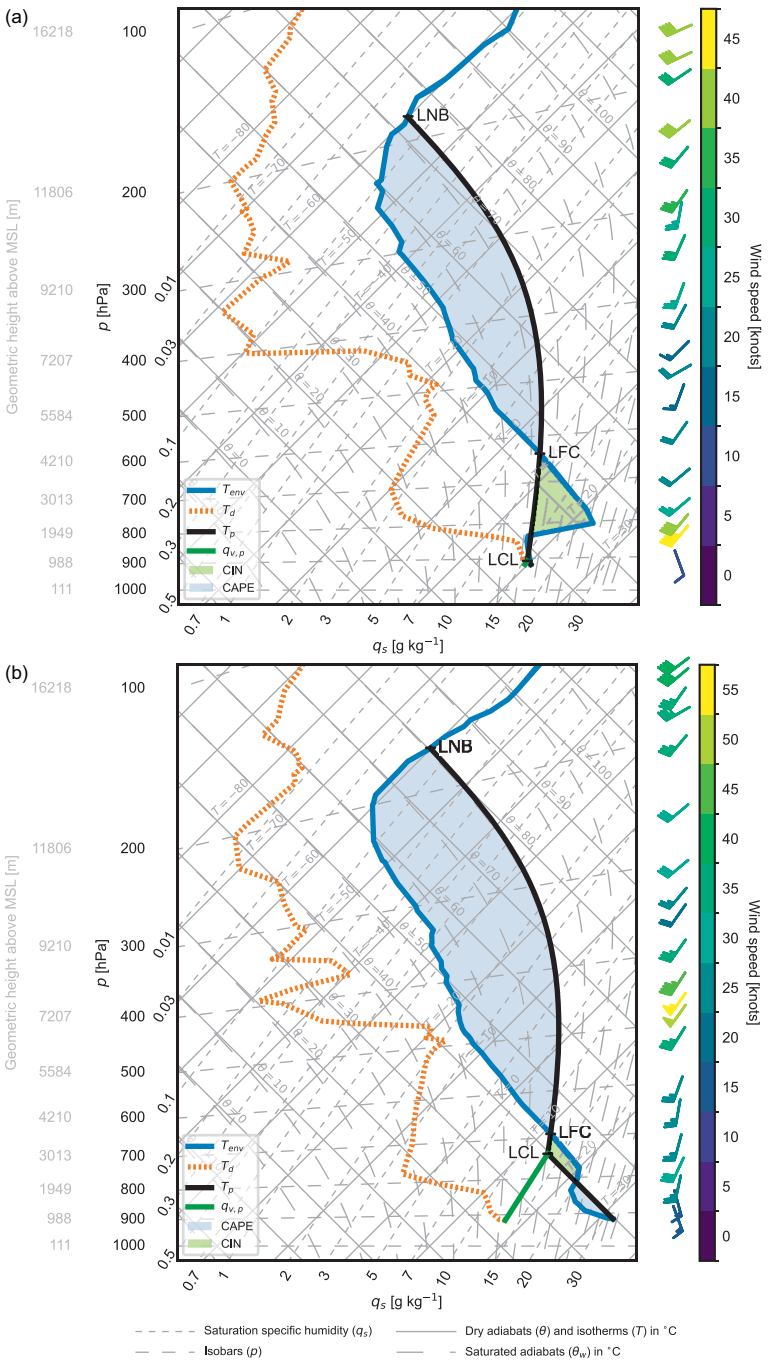


Figure 11.13 Tephigrams showing profiles of T_{env} (blue lines), T_d (orange lines), the air parcels' ascent T_p (black line) and wind barbs (colored) in an environment that produced a tornadic supercell storm in Kansas, USA. The soundings were taken at Dodge City, Kansas on May 18, 2013 at 7:00 (a) and 13:00 (b) local time. Data were obtained from the National Climate Data Center in the United States.

https://doi.org/10.1017/9781009485654.012 Published online by Cambridge University Press

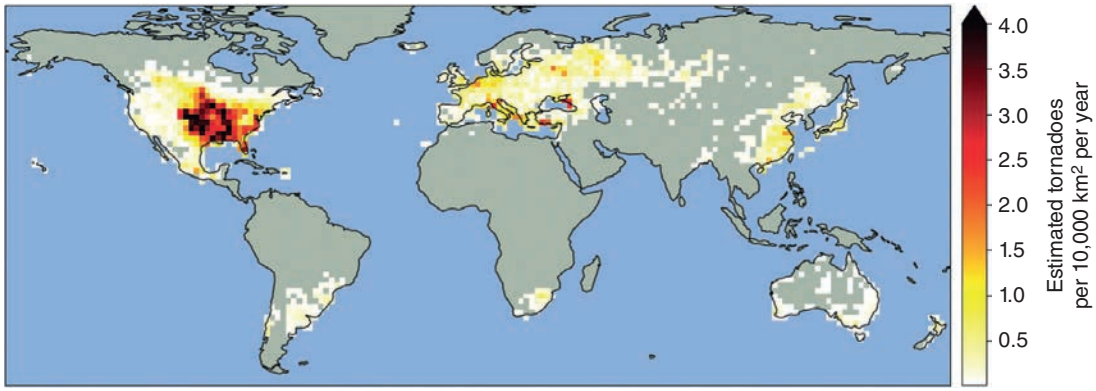


Figure 11.14 Estimated global distribution of annual tornado frequency per 10 000 km^2, using a 2 ° bin size. An online user interface for further exploring the entire tornado data base is available at https://tornadoarchive.com/explorer/. Figure taken from Maas et al. (2024). ©American Meteorological Society. Used with permission.

category (EF5 on the enhanced Fujita scale). For comparison, on average less than one EF5 tornado is observed per year. This tornado outbreak was accompanied by supercells with CAPE values between 2500 and 3000 J kg^{-1} originating from quasi-linear convective systems (Section 11.3) and long-lived supercell storms (Knupp et al., 2014). Prior to this event, the record number of tornadoes had been counted during the historic 1974 tornado outbreak, where between April 3 and April 4, 148 tornadoes were recorded across 13 states of the USA[13].

Tornadogenesis remains challenging to forecast as only one quarter of all mesocyclones are associated with tornadoes (Trapp et al., 2005b). One reason for the forecasting challenge of tornadoes is that they occur on the microscale (Figure 1.24) and that differences in relative humidity and low-level wind shear are often too localized to be detectable by the observation network. Therefore, often only slight differences exist between radiosoundings from locations in the proximity of tornado formation and those where tornadoes actually form (Maddox, 1976).

The global map in Figure 11.14 shows an estimated frequency distribution of the annual tornado occurrence (Maas et al., 2024). Areas with high tornado genesis are the United States, in particular the eastern and central US, and the northern Mediterranean coast. The tornado activity is highest in the spring and summer of the respective hemisphere (Maas et al., 2024).

11.3 Mesoscale Convective Systems

MCSs are the largest convective storms. The name MCS indicates that they develop mesoscale (Figure 1.24) circulations as they mature. An MCS is defined as an organized cloud system that occurs in connection with an ensemble of convective storms and produces a contiguous precipitation area on the order of 100 km or more in at least one horizontal direction[14]. They

[13] https://en.wikipedia.org/wiki/1974_Super_Outbreak
[14] https://glossary.ametsoc.org/wiki/Mesoscale_convective_system

https://doi.org/10.1017/9781009485654.012 Published online by Cambridge University Press

occur on the meso-α scale (Section 10.4) and are even larger and longer lasting than individual multicell or supercell storms. MCSs have lifetimes of 6–12 h. Detailed reviews of MCSs are provided by Houze (2004), Cotton et al. (2011), and Laing (2015).

MCSs encompass midlatitude *squall lines* (also called *multicellular line storms*), *bow echoes*, *mesoscale convective complexes* (MCC), tropical squall lines, and non-squall clusters, small multicellular storms, and even some tropical cyclones (Laing, 2015). MCSs account for a large portion of precipitation in the tropics, as well as during the warmer half of the year in midlatitudes (Nesbitt et al., 2006; Roca et al., 2014). For example, 30–70 % of the precipitation in the Great Plains and midwestern United States was found to result from MCSs between April and September (Fritsch et al., 1986). MCSs also account for more than 20 % of the tornadoes formed and 10 % of the severe hail reports in the central and eastern United States (Ashley et al., 2019). Characteristic of an MCS is the coexistence of convective and stratiform precipitation (Houze Jr., 1989). The convective regions are characterized by vertically extending cores associated with buoyant updrafts and downdrafts, characterized by high radar reflectivities from large hydrometeors. The stratiform regions are spatially more uniform and associated with considerably lower reflectivities and lighter precipitation. This stratiform precipitation forms as a result of the dissipation of older convective cells and the sloped ascent of a mesoscale layer of air.

Here we restrict our discussion to QLCSs (Section 11.3.1) and MCCs (Section (11.3.2). A QLCS is defined as an MCS that must be at least three times as long as it is wide (Ashley et al., 2019) with instantaneous convective regions ($Z \geq 40$ dBZ) that are longer than 100 km (typically with length scales of 1000 km along the line). The most common type of QLCSs are squall lines (Section 11.3.1).

11.3.1 Quasi-linear Convective Systems: Squall Lines

Squall lines are composed of groups of deep convective cells (multicells) arranged in a narrow band or line, and typically form along cold front boundaries. Because of their large horizontal extent, and their frequent occurrence in association with an upper-level trough, they are easier to forecast than smaller convective storms. For instance, squall lines (Figure 11.15) often form behind a long continuous gust front. The gust front can coincide with a cold front of a low pressure system. These linear MCSs can be further distinguished into those in which the stratiform precipitation occurs ahead of the convective precipitation (leading stratiform), parallel to it (parallel stratiform), or behind it (trailing stratiform) (Parker and Johnson, 2000). A cross section through an idealized midlatitudinal squall line that is moving eastward is shown in Figure 11.16 (Houze, 1993). The air generally ascends from the front to the rear through the squall line, as indicated by the solid red arrows. In the direction of the storm motion, warm air is lifted above the surface gust front, causing the formation of a new convective cell. The new cell is followed by a mature convective cell and an old cell. This internal structure is revealed by the radar echo, which for squall lines is typically characterized by a strong reflectivity gradient along the leading edge of the storm.

Strong radar echoes are associated with the mature and old cell, which are characterized by heavy convective showers. The precipitation drops immediately behind this line of active

https://doi.org/10.1017/9781009485654.012 Published online by Cambridge University Press

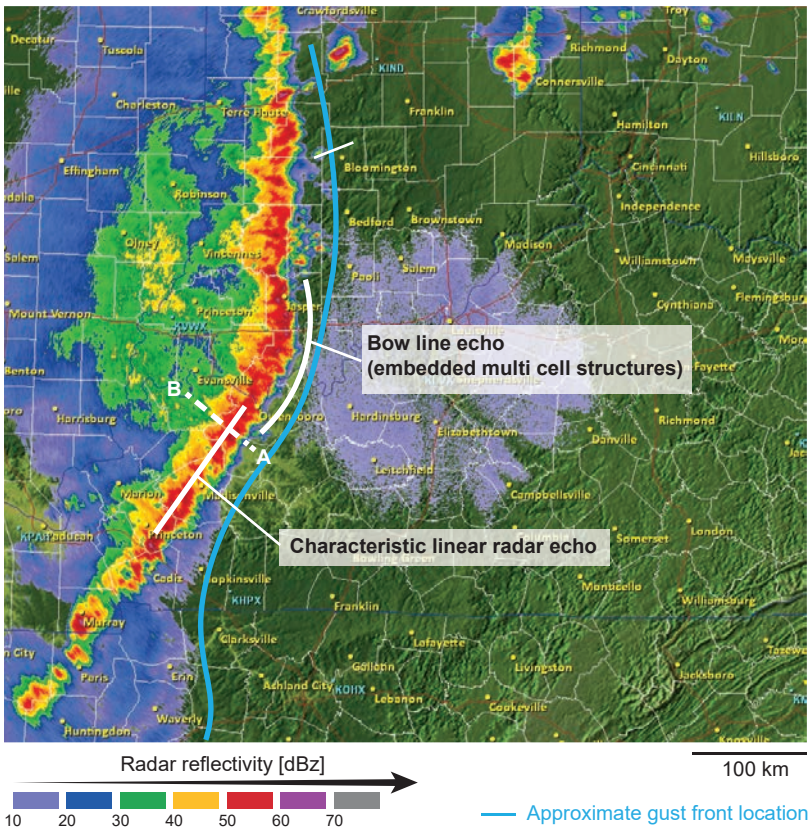


Figure 11.15 Radar image of a squall line (band of high radar reflectivity). A typical vertical cross section from points A to B through the squall line is shown in Figure 11.16. Radar image taken from www.nssl.noaa.gov/education/svrwx101/thunderstorms/-types/.

convective cells, but is followed by a secondary maximum that corresponds to the trailing stratiform precipitation falling from older cells. The case of trailing stratiform precipitation fields behind the convective line, as shown in Figure 11.16, has been identified as the most common case for (midlatitudinal) squall lines (Parker and Johnson, 2000). The ascent of the mature convective cell is terminated once it reaches the tropopause and spreads out horizontally, mainly downwind of the storm motion. This mechanism is the same in every Cb that has a noticeable horizontal anvil.

Also shown in Figure 11.16 are the characteristic microphysical processes associated with a squall line. The anvil at the rear is fed by ice crystals (dotted trajectories) initially formed inside the mature convective cells, which are transported by the ascending front-to-rear flow. In fact, a large fraction of the hydrometeors within the stratiform anvil cloud results from the region of active convection within the squall line. For instance, Gamache and Houze (1983) found that (horizontal) transport of hydrometeors from the convective towers contributes about 60–75 % of the mass of the hydrometeors within the stratiform region.

First, cloud droplets grow by collision–coalescence in the updraft of the convective core. Upon freezing, the frozen hydrometeors continue to grow by aggregation, and riming (Figure 11.16). After reaching the stratiform region, the ice crystals continue to grow by deposition. Growth by aggregation and riming becomes important in the vicinity of the melting layer.

https://doi.org/10.1017/9781009485654.012 Published online by Cambridge University Press

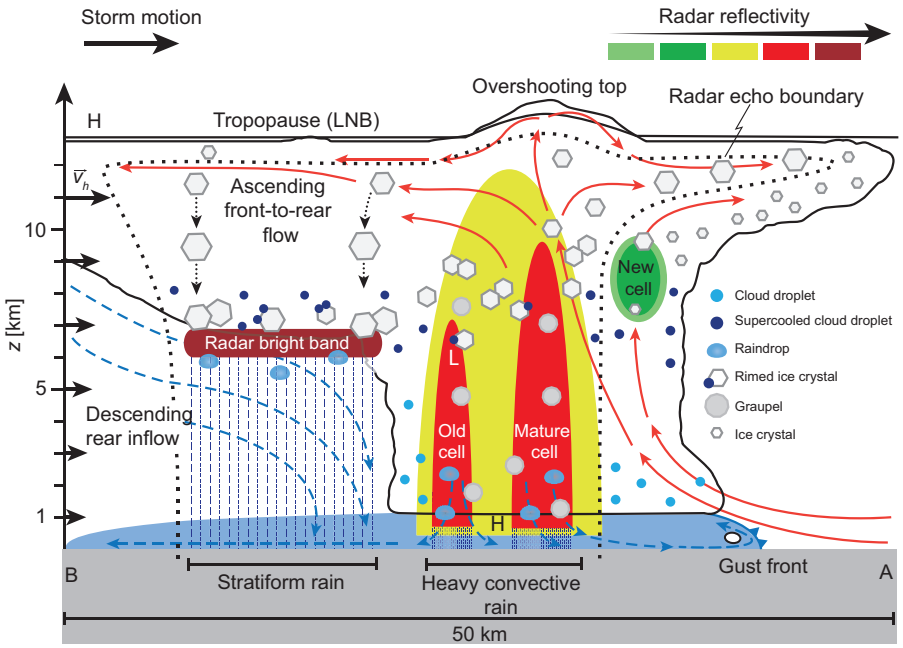


Figure 11.16 Conceptual model of the characteristic air flows, microphysical processes, and radar-echo structure of a squall line with a trailing stratiform cloud layer, viewed as a vertical cross section oriented perpendicularly to the squall line and parallel to its motion. Different radar reflectivities are indicated by the differently colored shadings, and the radar-echo boundary by the dotted line. The small horizontal red area in the stratiform region denotes the radar bright band (melting layer) (Section 10.3.3). The points labeled H and L indicate centers of positive (high) and negative (low) pressure perturbations. The solid red arrows indicate the updraft and outflow inside the squall line, and the broken blue arrows indicate the downdrafts and descending rear inflow. Also shown are hydrometeors, characteristic for the cloud microphysical processes in the squall line. The dotted black arrows indicate typical ice particle trajectories. The labels A and B along the surface correspond to the points along the cross-sectional line shown in Figure 11.15. Figure adapted from Houze et al. (1989) ©American Meteorological Society. Used with permission.

This layer constitutes the radar bright band (horizontal red area). Below the radar bright band, stratiform precipitation leaves the MCS. It is, however, more intense than typical stratiform rain as a result of the seeder–feeder mechanism (Section 10.5.3) that is triggered by the convective core.

In addition to heavy rain, a squall line frequently produces lightning, strong straight-line winds and possibly, landspouts (non-supercell tornadoes over land) or waterspouts (non-supercell tornadoes over water). Waterspouts and landspouts are typically less violent than supercell tornadoes. The strong straight-line winds associated with squall lines are often referred to as *derechos* (Johns and Hirt, 1987; Hinrichs, 1888; Corfidi et al., 2016). Wind speeds in derechos can exceed 160 km h^{-1} and cause considerable damage to infrastructure.

https://doi.org/10.1017/9781009485654.012 Published online by Cambridge University Press

11.3.2 Mesoscale Convective Complexes

MCCs are meso-α-scale MCSs with a large, quasi-circular cold cloud shield, allowing their identification in (infrared) satellite images according to their low cloud top temperature. Specifically, an MCC is defined as having cloud top temperatures below $-32\,^{\circ}\mathrm{C}$ over an area of $100\,000\,\mathrm{km}^2$ or cloud top temperatures below $-52\,^{\circ}\mathrm{C}$ over an area of $50\,000\,\mathrm{km}^2$ for at least 6 h (Maddox, 1980). In satellite images, MCCs appear as fairly round cloud systems with an eccentricity (the ratio of the minor and the major axis) of at least 0.7 at their maximum extent.

Based on these criteria, 75 % of the 16 MCSs studied in Oklahoma–Kansas in 1985 were identified as MCCs (Loehrer and Johnson, 1995). A global climatology of 714 MCSs found that the cold-cloud shield covered an average area of about $350\,000\,\mathrm{km}^2$ and the MCSs had an average lifetime of 10 h. The same study found that with about 400 MCCs occurring globally per year, the majority (91.6 %) forms over land, and that two-thirds of the MCCs are found in the northern hemisphere between the equator and 50 °N (Laing and Fritsch, 1997).

MCCs can cause heavy rainfall and severe weather, and they are a fundamental component of the Indian monsoon (Laing and Fritsch, 1993). Average precipitation rates in MCCs on the order of $10\,\mathrm{mm\,h^{-1}}$ have been reported (McAnelly and Cotton, 1989), with peak precipitation rates over $25\,\mathrm{mm\,h^{-1}}$ (Laing, 2015). These precipitation rates occur over large areas (Kane et al., 1987) and overall, the rate of extreme rainfall generated by MCCs is larger than that from any other source (Laing, 2015).

MCCs form in baroclinic zones and need locally high values of lower-tropospheric wind shear and CAPE. The high values of CAPE are typically caused by a low-level jet that is oriented nearly perpendicular to the baroclinic zone and advects air with low static stability and high values of θ_e (Laing and Fritsch, 2000). While for supercells typically the shear is measured within the lowest 6 km from the surface, for MCCs, the shear must be present between 1000 and 700 hPa (Laing and Fritsch, 2000). The CAPE values upon MCC genesis vary between 1300 and 2900 $\mathrm{J\,kg^{-1}}$ in different parts of the world (Laing and Fritsch, 2000).

11.4 Hail and Lightning

Convective storms are often accompanied by hail as well as lightning and thunder. There are generally four different types of lighting: cloud-to-cloud, intra-cloud, cloud-to-air, and cloud-to-ground (Paras and Rani, 2018). Lightning requires the simultaneous presence of an ice and a liquid phase inside a cloud and also that the cloud top is colder than $-15\,^{\circ}\mathrm{C}$. Both criteria are met in cumulonimbus clouds. Lightning describes the high-current electrostatic discharge of thunderstorm clouds and is an important part of the global electrical circuit (Section 11.4.3). In the lightning channel, the temperature can reach up to 30 000 K as a result of the charge transfer (Section 11.4.5), and it is accompanied by a pressure enhancement of one to two orders of magnitude, resulting in a sound wave (thunder). Lightning activity is often closely associated with hail (Changnon, 1992; Farnell et al., 2018).

11.4.1 Hail

Convective storms with large CAPE can produce hail if the following three prerequisites are met: (i) *Hail embryos* must be abundant. A hail embryo can either be a graupel particle or a

https://doi.org/10.1017/9781009485654.012 Published online by Cambridge University Press

frozen drop (Knight and Knight, 1970). While frozen drop embryos dominate at cloud base temperatures above −10 °C, convective storms with lower cloud base temperatures are dominated by graupel embryos (Lamb and Verlinde, 2011). (ii) A sufficient amount of supercooled liquid water must exist in the cloud, ensuring that the hailstone can grow by riming, and (iii) a strong and wide updraft within the convective storm must exit. Updrafts promoting hail growth typically exceed 15 m s^{-1} (Raupach et al., 2021). Wide (spatially broader) updrafts result from increased vertical wind shear (Mulholland et al., 2021, 2024) and provide a larger volume of the storm that is conducive to hailstone growth.

A hailstone is defined as a rimed particle that is larger than 2.5 mm in radius (Table 1.2). The largest recorded hailstone fell in a convective storm in South Dakota, USA, on July 23, 2010. It had a diameter of 20.32 cm and weighed 0.88 kg[15]. The heaviest recorded hailstone was found in Bangladesh in April 1986 with 1.02 kg[16].

The typical growth and life cycle of a hailstone originating from a frozen drop embryo is shown schematically in Figure 11.17. Normally, a raindrop forms first (labeled point 1 in Figure 11.17). Because of the strong and wide updrafts associated with convective storms in which hail is formed, the raindrop is lifted far above the 0 °C level, where it freezes and acts as the embryo of the hailstone (point 2 in Figure 11.17). It grows further by collisions with cloud droplets and ice crystals in the updraft until it becomes heavy enough to fall down (point 3). On its way down (between points 3 and 4 in Figure 11.17), it grows by further colliding with ice particles and supercooled cloud droplets and raindrops.

Hailstones often exhibit a layered internal structure that corresponds to alternating layers of clear and milky (opaque) ice (Macklin, 1962; Browning, 1966). To develop this layered

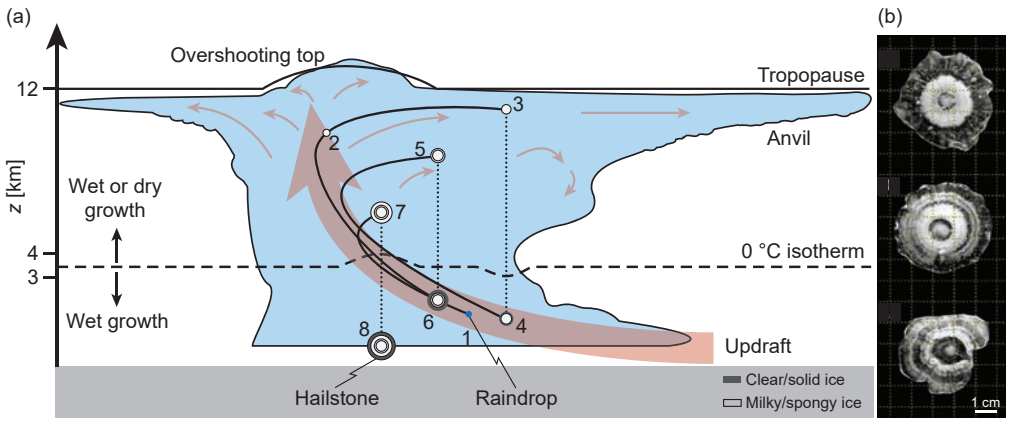


Figure 11.17 (a) Schematic of hailstone formation. Black circles denote wet growth and white circles dry growth. Upward directed motions of the hailstone are denoted by solid lines and downward motions by dotted lines. The altitudes on the *y*-axes denote typical values for midlatitudes summer convective storms. Melting layer height is based on Dessens et al. (2015). (b) Examples of hailstone cross-sections, where dark and white regions indicate clear (solid) and opaque (spongy) ice, respectively. Grid lines are shown at a spacing of 1 cm. Images taken from Soderholm and Kumjian (2022).

[15] www.weather.gov/abr/vivianhailstone
[16] http://wmo.asu.edu/#global

https://doi.org/10.1017/9781009485654.012 Published online by Cambridge University Press

structure, the hailstone has cycled several times through wet and dry growth regimes. This cycle is typically achieved if the hailstone is carried upward in the cloud multiple times and thereby crosses the 0 °C isotherm repeatedly: the second time the hailstone enters the updraft is point 4 in Figure 11.17. In the updraft, the liquid shell freezes. Again, at some point, the hailstone becomes too heavy to be carried further upward and falls down again. Between points 5 and 6, it grows again by collisions with ice particles and cloud droplets. This cycle is repeated until the hailstone no longer enters an updraft or is too heavy to be carried upwards by the updraft and falls down to the surface (from point 7 to 8 in Figure 11.17), possibly colliding with further cloud droplets and/or raindrops on its way.

Cloud droplets or raindrops colliding with the hailstone can form a liquid shell around the frozen core, even if the droplets are supercooled. If the temperature at the hailstone surface exceeds 0 °C, the collected cloud droplets form a liquid layer around the hailstone. Even when a hailstone collides with supercooled liquid cloud droplets at $T < 0\,°\mathrm{C}$, a liquid layer can still form from the release of the latent heat of fusion by the freezing process. In this case, thermal energy may not be fully dissipated to the environment, causing the hail surface to become liquid. The temperature of the hailstone remains at 0 °C as long as the hailstone still has ice that can melt or as long as latent heat of fusion is released by the freezing process. How much supercooling a hailstone can tolerate and still form a liquid layer depends on its size and density. It also depends on the size and number concentration of the hydrometeors with which it collides, which in turn is determined by the cloud's liquid water content and air temperature (List, 2014). In laboratory studies, a liquid shell around the hailstone was observed down to −10 °C (Garcia-Garcia and List, 1992). In this so-called *wet growth* regime of the hailstone, the air dissolved in the water of the hydrometeors collected by the hailstone has sufficient time to escape during the freezing process, leading to clear, solid, ice layers.

In contrast, if growth involving collision of the hailstone with ice crystals and/or supercooled cloud droplets occurs while the temperature of the hailstone remains well below the freezing point, and all accreted water freezes, the growth is called *dry growth* (Lesins and List, 1986; List, 2014). In the dry growth regime, freezing is so fast that the collected supercooled droplets do not have time to spread over the entire surface of the hailstone, thus leaving the hailstone surface dry. In addition, the rapid freezing does not permit the dissolved air to escape to the environment, such that the air bubble concentration increases for larger freezing rates (Carte, 1961; Carras and Macklin, 1975). These air inclusions cause the ice to have a porous structure and to appear milky. This ice is also referred to as *spongy ice* and has a lower density than the bubble-free solid ice. If the hailstone is dominated by solid ice, its density can exceed $800\,\mathrm{kg\,m^{-3}}$ (Table 1.2 and Straka and Mansell (2005)).

11.4.2 Hail Suppression

Hail damage increases overproportionally with the size of the hailstones. Hailstones exceeding a radius of 1 cm can cause severe damage to agriculture and infrastructure. Artificial weather modification with the purpose to suppress hail damage aims at limiting the size of the hailstones by the method of *beneficial competition* (Knight et al., 1979; Spiridonov et al., 2015). This method seeks to distribute the available supercooled liquid water over as many

https://doi.org/10.1017/9781009485654.012 Published online by Cambridge University Press

hail embryos as possible to enhance their competition for the supercooled liquid water and by doing so attempt to reduce their growth. To achieve this effect, AgI particles are injected into developing hail storms to act as INPs. These injected INPs should reach the main hail growth region, which is the area where temperatures are between −25 and −10 °C. This can be achieved either by generators and flares from the ground in an area-wide network (Dessens et al., 2016) or from aircraft (Wieringa and Holleman, 2006), which can target the main hail growth zone more directly.

Hail seeding is still subject to many uncertainties, and so the results of field and modeling studies on hail suppression diverge. Some studies find no significant differences due to seeding (Federer et al., 1986; Milivoj B. Gavrilov and Gavrilov, 2010), others see a decrease in hail concentration and/or size (Simeonov, 1996; Dessens et al., 2016; Oppenländer et al., 2022). Hail seeding will only be successful if the seeding material reaches the hail formation zone at the initial stage of the developing storm. If not, more and/or larger hailstones may form than would have formed without seeding, or seeding may simply have no effect because the region with supercooled cloud water is not the one in which the hail embryos form. The different results of the field studies and the modeling studies (Ćurić, 2007; Papaevangelou et al., 2025) clearly show that meteorological variability makes it difficult to obtain a clear statistical signal of the success or failure of hail suppression.

11.4.3 Global Electrical Circuit

For the occurrence of lightning, a separation of charges either within the cloud (inter-cloud lightning), between clouds (intra-cloud lightning), or between the cloud and Earth surface (cloud-to-ground lightning) is required. A typical charge distribution in a mature thunderstorm and its role in the global electrical circuit, are shown in Figure 11.18. It illustrates the distribution and transport of charges between the main components of the global electrical circuit. According to convention, the global electrical circuit is shown for the propagation direction of the positive charges. Negative charges, in the form of free electrons, flow in the opposite direction.

Earth's atmosphere has a downward-directed electrical field, which carries a net positive charge from high to low altitudes, termed the *fair weather current*. Its upper extent is bounded by the *electrosphere*. The electrosphere is a layer of the atmosphere that begins a few tens of kilometers above Earth's surface and extends upwards, up to the *ionosphere*[17]. In the electrosphere, the electrical conductivity is so high that the layer essentially carries a constant electric potential. Together, the electrosphere and Earth's surface resemble a charged capacitator, that is, two oppositely charged electrodes, with an insulator (atmospheric layers) in between. The mean potential of the positively charged electrosphere relative to the negatively charged Earth's surface is about 250 kV (Wallace and Hobbs, 2006), corresponding to about 1000 domestic power outlets. The electrical conductivity increases with altitude due to the increasing ionization by *cosmic rays*. Cosmic rays denote the extra-terrestrial radiation, mainly

[17] https://glossary.ametsoc.org/wiki/Electrosphere

https://doi.org/10.1017/9781009485654.012 Published online by Cambridge University Press

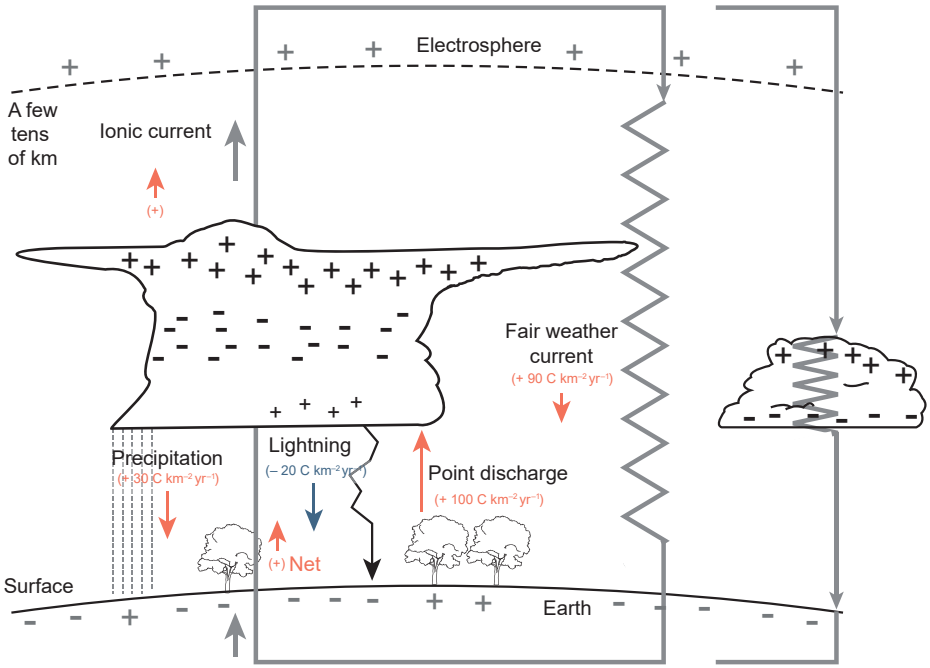


Figure 11.18 Schematic of the main global electrical circuit (not to scale). The positive and negative signs in parentheses indicate the sign and approximate amount of the transported charges for the main components of the global electrical circuit. Charges leave the charge-separated regions in the thunderstorm and return to the surface through the electrical resistance of the atmosphere (fair weather current). In some cases, the current returns to the surface through layer clouds (Harrison and Nicoll, 2022), as shown on the right. The system can be regarded as an electrical circuit, illustrated by the bold gray lines, in which the thunderstorm clouds act as the generators, transporting charge between the electrosphere and Earth's surface. The relative resistance of cloud and clear air regions is illustrated by compressed and stretched resistor symbols, respectively.

composed of high-energy protons, that continuously bombard Earth's atmosphere, influencing the global electrical circuit and also climate (Kirkby, 2007). The electrical conductivity peaks in the ionosphere, which extends from approximately 85 to 600 km above Earth's surface. The ionosphere consists of electrons and electrically charged atoms and molecules, and has a peak electron density at around 300 km. Above 300 km, the electron density decreases again because of the decrease in air density with increasing altitude.

One source of the net positive charge of the electrosphere is the positive charge that leaks from the upper, positively charged levels in thunderstorms into the base of the electrosphere via the so-called *ionic current*, as indicated in Figure 11.18. Below the thunderstorm base, the so-called *point discharge current* transports positive charge from trees and obstacles at Earth's surface to the cloud base.

The base of the fair weather current is bounded by Earth's surface. Earth's surface usually carries a net negative charge. The reason for this is that lightning carries negative charges from

https://doi.org/10.1017/9781009485654.012 Published online by Cambridge University Press

the main negative charge region in the cloud to Earth's surface. At the same time, hydrometeors are polarized by the electric field of the fair weather current, as well as by the electric field beneath thunderstorms in such a way that they tend to preferentially collect positive ions as they fall to the ground (Wallace and Hobbs, 2006). Therefore, they transfer positive charges to Earth's surface.

An approximate charge budget of the global electrical circuit is indicated in Figure 11.18. From the electrosphere, the fair weather current continuously leaks a positive charge of $90\,\mathrm{C\,km^2\,yr^{-1}} = 1456\,\mathrm{A}$ to Earth's surface (Pruppacher and Klett, 1997; Wang, 2013). About $30\,\mathrm{C\,km^2\,yr^{-1}}$ of positive charge reaches Earth's surface by precipitation, while $100\,\mathrm{C\,km^2\,yr^{-1}}$ of positive charges are lost by point discharge. In addition, about $20\,\mathrm{C\,km^2\,yr^{-1}}$ of negative charges reach the Earth by ground flashes (Wallace and Hobbs, 2006). Globally, there are approximately 12–16 ground flashes every second with a maximum rate of $55\,\mathrm{s^{-1}}$ over northern hemisphere land masses in summer. Each lightning strike carries a charge of more than 20 C (Wallace and Hobbs, 2006). Thus, lightning supplies Earth's surface with negative charges of $1500\,\mathrm{A} = 1500\,\mathrm{C\,s^{-1}}$ (corresponding to the current of 150 electric kettles), in order to balance the fair weather current and the positive charges carried to the surface by precipitating hydrometeors. Assuming a current of 1 A per thunderstorm cell (Pruppacher and Klett, 1997), there are globally $\sim$ 1500 thunderstorm cells active at any one time.

Overall, the electric field of Earth's atmosphere is almost constant, despite the capability of the fair weather current to discharge the potential existing between the electrosphere and Earth's surface. In fact, in the global electrical circuit, thunderstorm clouds are the electrical generators, or batteries, of the circuit, which continuously transport charges between Earth's surface and the electrosphere.

11.4.4 Charge Separation Within Clouds

For lightning to occur, the charges inside the cloud need to be separated. The typical assumption is that before lightning occurs, a Cb cloud has a tripole charge structure, with positive charges near the cloud top and the cloud base and a negative charge region in the center (Williams, 1989). The negatively charged layer in the middle of the cloud is called the *main charging zone*. It typically occurs between the -10 and $-20\,^{\circ}\mathrm{C}$ isotherms as illustrated in Figure 11.19, but varies with the type of the convective system (Stolzenburg et al., 1998).

Different hypotheses exist on how charge separation occurs and the exact conditions are still a matter of debate. Here we will focus on the (i) thermoelectric and (ii) diffusional growth theories. A review of these and other possible charge separation mechanisms is given, for example, by Saunders (2008).

(i) The thermoelectric theory was one of the first mechanisms proposed to account for the charge separation based on early laboratory experiments, where charge exchanges were observed during collisions of cloud particles (Reynolds et al., 1957). More specifically, rebound collisions, where the involved hydrometeors do not remain together after the collision, between graupel particles and ice crystals at different temperatures inside the Cb initiate the exchange of charge and generation of charge separation (Dash and Wettlaufer, 2003). The exchange

https://doi.org/10.1017/9781009485654.012 Published online by Cambridge University Press

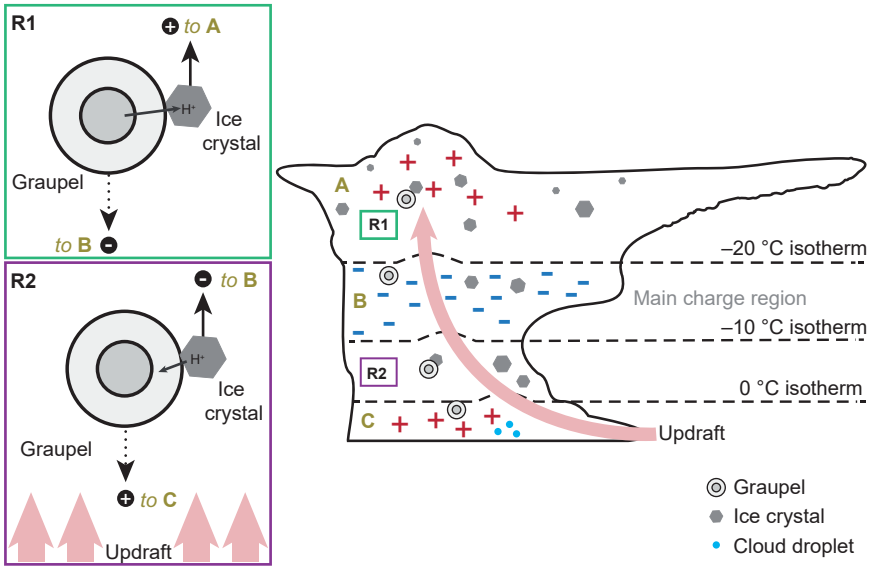


Figure 11.19 Schematic view of the generation of charge separation within thunderstorm clouds involving the collision of an ice crystal with a graupel particle. At lower temperatures, the graupel particle becomes negatively charged (region R1), while at higher temperatures, the graupel becomes positively charged (region R2). The charge separation results from the differing terminal velocities of oppositely charged hydrometeors being transported into different regions (A, B, C) of the cloud, ultimately resulting in the characteristic tripole charge structure of Cb clouds.

and separation of charges occur because of the different temperatures and different terminal velocities of oppositely charged hydrometeors, as shown in Figure 11.19.

Within the region of the cloud marked as R1, the graupel or hailstone falls against the updraft and collides with ice crystals along its trajectory. The surfaces of the graupel particles or hailstones are warmer than those of the ice crystals because they collide with (supercooled) liquid droplets, which freeze upon contact and thereby release latent heat. Upon collision of the hailstone or graupel particle with the ice crystal, H^+ ions, which in ice diffuse more rapidly than OH^- ions (Eigen et al., 1958), move from the relatively warmer hailstone or graupel particle to the colder colliding ice crystal. This causes the warmer graupel particle to become negatively charged (Reynolds et al., 1957). The magnitude of the charge transferred per collision depends on various factors such as temperature and relative velocity, but is typically on the order of 0.25–10 fC (Jayaratne et al., 1983; Wallace and Hobbs, 2006). As the small positively charged ice crystals are carried upward with the updraft within the cloud, a charge separation between the layer of negative charges in the middle of the cloud (region B) and the positively charged region in the upper layers of the cloud (region A) is established (Figure 11.19).

The early experiments by Reynolds et al. (1957) focused on the negative charging of the graupel particles at a temperature around −25 °C. Other studies have reported that the charge sign of the hailstone or graupel could be positive or negative, depending on the temperature and

https://doi.org/10.1017/9781009485654.012 Published online by Cambridge University Press

LWC in the cloud (Takahashi, 1978). While at higher altitudes and lower cloud temperatures, the graupel becomes negatively charged, at lower altitudes and higher cloud temperatures, the separation of charges reverses so that the graupel becomes positively charged (inset for R1 vs. R2 in Fig. 11.19). In this case, the falling positively charged graupel particles contribute to the positively charged region at cloud base (region C), while the negatively charged ice crystals are carried within the updraft and contribute to the negative charge in the cloud center (region B).

(ii) Other theories relate the charge separation within Cb clouds to differences in the diffusional growth rates of graupel particles and ice crystals (Baker et al., 1987; Saunders et al., 2006; Glassmeier et al., 2018). According to this theory, if the graupel particle surface is growing more rapidly from the vapor phase compared to the ice crystal surface, then graupel particles become net positively charged upon collision (Baker et al., 1987). Water vapor deposition causes latent heat release and increases the temperature at the hailstone's surface. Then, the positive ions to move down the temperature gradient toward the center of the hydrometeor, leaving its surface negatively charged. Upon collision, the negative charge is then transferred to the hydrometeor with the slower growth rate (Wallace and Hobbs, 2006). It remains unclear whether the diffusional growth rate theory can explain the tripolar structure observed in most thunderstorm clouds. Therefore, the charge structure in thunderstorms may not be explained by a single charge separation mechanism, but different mechanisms could be important in different regions of the cloud.

11.4.5 Cloud-to-Ground Lightning

Separation of charges within a cloud leads to a strong potential difference between the upper and lower parts of the cloud as well as between the cloud and the Earth's surface, ultimately causing the generation of a strong electric field. This is often referred to as thunderstorm electrification. Once this electric field is stronger than the so-called *breakdown field strength* ($>$ 100 to 350 $\mathrm{kV\,m^{-1}}$, with higher values at higher air densities/lower altitudes, Stolzenburg and Marshall, 2009), lightning is likely to occur in order to equilibrate the charge difference. In this case, the electric field is strong enough to locally ionize the air within a small channel. This is associated with a strong increase in the conductivity of the air within this channel. Charge transport then preferentially occurs through this channel, and is visible as lightning.

Here we focus on cloud-to-ground lightning flashes, also termed *ground flashes*. These account for only 25 % of all lightning flashes (Paras and Rani, 2018). Cloud-to-ground lightning flashes are more common in midlatitudes than in the tropics, where only 10 % of all lightning flashes are ground flashes (Pierce, 1970). Possible explanations are that this is caused by the 0 °C isotherm being at higher altitudes in the tropics (Pierce, 1970), or that the thickness of the cold cloud region (region between 0 °C and cloud top) is larger in the tropics (Price and Rind, 1993). In either case, the main charging zone (Figure 11.19) occurs at higher altitudes in the tropics. Several strokes are needed to equalize the charges between the thunderstorm cloud and Earth's surface, taking on average three to four strokes per lightning flash.

Most cloud-to-ground lightning strokes transport electrons from the cloud to the ground while the return strokes carry positive charges from objects at Earth's surface to the cloud base, as illustrated in Figure 11.20 (Uman, 1987) and highlighted in the photograph shown

https://doi.org/10.1017/9781009485654.012 Published online by Cambridge University Press

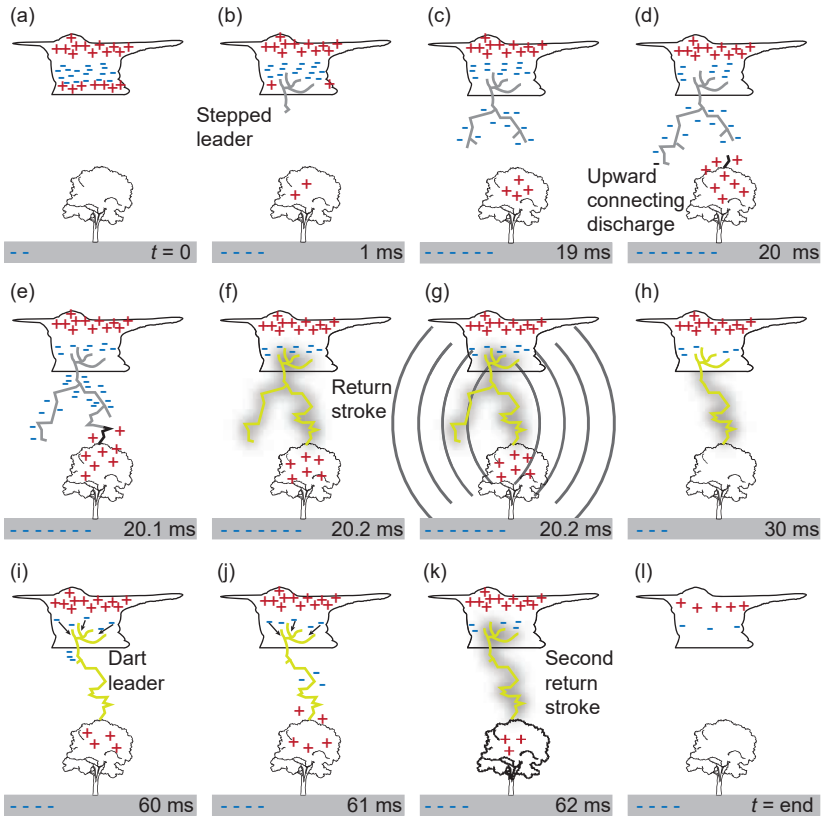


Figure 11.20 Schematics (not to scale) illustrating processes leading to a ground flash and their associated time steps: (a) cloud charge distribution, (b) preliminary breakdown, (c, d) stepped leader, (e) attachment process, (f, h) first return stroke, (g) thunder, (i, j) dart leaders of subsequent strokes, (k) second return stroke, and (l) situation after the lightning strokes have finished. The visible strokes (f, k) are shaded. Figure adapted from Uman (1987) with permission from Elsevier.

in Figure 11.21. Ground flashes that transport negative charges to the ground originate from the lower region of the negatively charged part of the cloud (Figure 11.20b). These negative cloud-to-ground lightning flashes account for about 90 % of the global downwards discharges, while about 10 % are positive cloud-to-ground lightning flashes that carry positive charge from the thunderstorm cloud to Earth's surface (Dwyer and Uman, 2014; Paras and Rani, 2018).

This discharge is initiated by the *stepped leader*. It moves downward toward Earth in discrete steps of 1 μs (~50 m, Figure 11.20c–e). Negative charge is continuously lowered from the main charge region of the thunderstorm cloud into the stepped leader channel, ionizing the path through which it propagates. The cascade nature of this process results from the electric field intensity at the tip of the stepped leader, which decreases as some electrons are captured by coagulation with positive ions, atoms, and neutral molecules within the air. These electrons then need to be replenished from higher levels.

https://doi.org/10.1017/9781009485654.012 Published online by Cambridge University Press

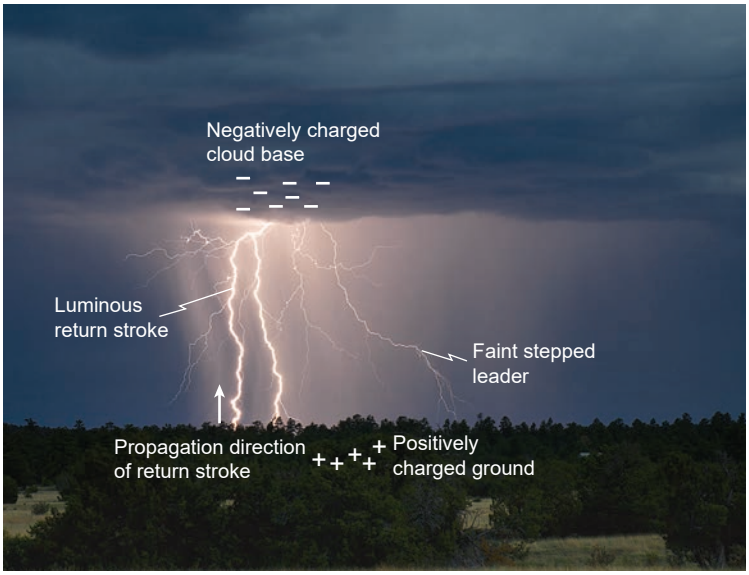


Figure 11.21 Photograph of a ground flash, in which some of the aspects of Figure 11.20 are highlighted. Note the branching of the stepped leader. Photograph taken by Dave Arnold Photo/Moment/Getty Images.

A typical process chain leading to ground flashes proceeds as follows (Wallace and Hobbs, 2006): The stepped leader is initiated by a local discharge between the lower part of the main negatively charged region of the cloud and a small pocket of positive charges at the base of the Cb (Figure 11.20b). Initially, the negative charges neutralize the pockets of positive charges at the cloud base and subsequently move toward the ground. As the negatively charged stepped leader approaches the ground, its electric field induces positive charges on high objects, such as tall buildings or trees (Figure 11.20c). Since opposite charges attract each other, the positive charge on the ground wants to combine with the negative charge within the stepped leader. When the stepped leader is within 10–100 m of the ground, a point discharge (Figure 11.18) moves up from the ground to meet it (Figure 11.20d). When this point discharge connects with the stepped leader (attachment process), the breakdown field strength is exceeded and a large number of electrons flow from the cloud to the Earth's surface (Figure 11.20e).

Afterwards, a highly luminous lightning stroke propagates upward from the ground to the cloud following the path of the stepped leader (Figure 11.20f), called the *return stroke*. The return stroke with its bright luminous channel is the stroke that is visible by the human eye. Because the return stroke propagates so fast, it appears as a simultaneously brightened channel between the ground and cloud base. Since a stroke only lasts a few milliseconds, the time is too short for the air to expand. Instead, the pressure increases almost instantaneously to values of 10–100 times the atmospheric pressure (Wallace and Hobbs, 2006). This simultaneously generates a cylindrical shock wave (Figure 11.20g), which propagates outward from the lightning channel faster than the speed of sound heard further away as thunder.

https://doi.org/10.1017/9781009485654.012 Published online by Cambridge University Press

Following the first return stroke, subsequent strokes can occur along the same main channel as long as the electric field remains sufficiently high. In this case, additional electrons are supplied by progressively more distant regions of the negatively charged area of the cloud. Another negatively charged leader, called the *dart leader*, then moves downward along the same path and carries further electrons to the ground (Figures 11.20c,j). In contrast to the first stepped leader, which usually has many branches, subsequent dart leaders usually have no branches and follow the main channel of the initial stepped leader (Figure 11.20f,k). The dart leader is followed by another visible return stroke to the cloud (Figure 11.20k). This process continues until the electric field is smaller than the breakdown field (Figure 11.20l). Then the charge separation process (Section 11.4.4) needs to start again, as a new electric field must be established before the next lightning sequence can occur.

The lightning flash of the first return stroke carries the largest current and reaches up to 40 kA, which heats up the channel by ohmic dissipation, energy loss caused by electrical resistance, to above 30 000 K. Hence, a lightning stroke is an atmospheric science example of a plasma, a mixture of free charge carriers containing free electrons and ions, as well as neutral atoms and molecules (Wang, 2013). This plasma, like the plasma in a neon lamp, emits light from relaxation of excited electrons, ions and molecules, making the lightning stroke visible.

The updraft speed in a convective cloud is a good indicator of the total lightning activity. An analysis of radar data from different thunderstorms in Colorado, Kansas, and northern Alabama, USA by Deierling and Petersen (2008) found a positive, linear correlation of $r \geq 0.92$ for the lightning rate and total updraft volume at temperatures lower than $-5\,°C$ and vertical velocities greater than $5\,m\,s^{-1}$. Less positive correlations were found between the lightning rate and maximum or mean updraft speed.

Hence, knowledge of the updraft speed in convective clouds can help to predict their lightning activity, which in turn is a good proxy for precipitation intensity. Besides its key role in the global electrical circuit, lightning is also important for the production of nitrogen oxides in the upper troposphere, affecting ozone concentrations, impacting overall atmospheric chemistry and climate (e.g., Banerjee et al., 2014).

11.4.6 Global Distribution of Hail and Lightning

The global distribution of lightning flashes per square kilometer for the period 1995–2002[18] is shown in Figure 11.22a and the probability of occurrence of hailstones larger than 1.25 cm in radius for the period 1979–2015 in Figure 11.22b (Prein and Holland, 2018). The distribution of lightning flashes has a noticeable land-sea-contrast and equator-pole-contrast with maximum lightning activity in areas with deep convection over land in the tropics. Lightning activity is favored over land because of the smaller heat capacity of land compared to oceans. A smaller heat capacity means that land surfaces, as compared to water surfaces, heat up faster during the day, and the atmosphere over land becomes more readily statically or conditionally unstable, initiating convective activity. Some of the hotspots for lightning activity

[18] https://earthobservatory.nasa.gov/images/6679/patterns-of-lightning-activity

https://doi.org/10.1017/9781009485654.012 Published online by Cambridge University Press

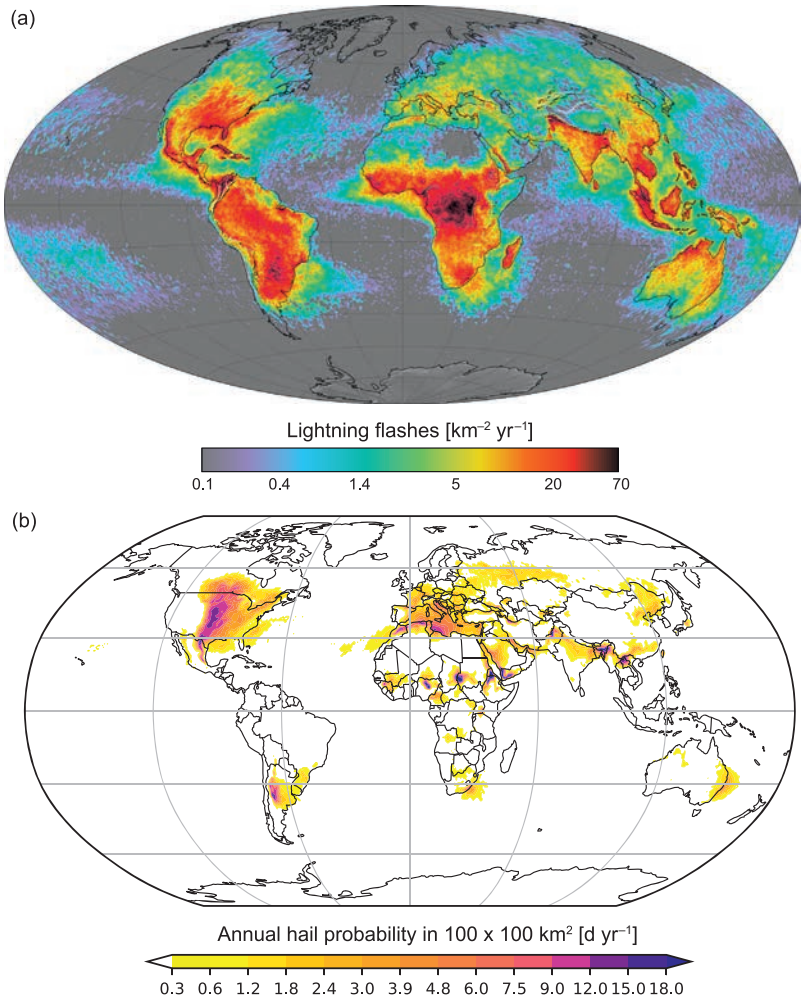


Figure 11.22 Global distribution of (a) annual lightning flashes per square kilometer using data collected by NASA satellites averaged over 1995–2002, and (b) the occurrence probability for hailstones >1.25 cm in radius for the period 1979–2015. Data: (a) obtained from NASA Earth Observatory image gallery at https://earthobservatory.nasa.gov/images/6679/patterns-of-lightning-activity, and (b) reproduced from Prein and Holland (2018).

also produce hail. However, hail is spatially much more limited than lightning. This is because the occurrence of severe hailstones (>1 cm in radius, Raupach et al., 2021) is mainly limited to multi- and supercells because of their typically larger and stronger updrafts (Table 11.1), while lightning commonly occurs also in ordinary convective storms. Thus, hotspots of hail often coincide with hotspots of supercells. These include the Great Plains in the USA and Canada, Central and West Africa, the Mediterranean regions of northern Africa and northern China. These regions are hotspots because they experience moist and warm air inflow in the boundary layer from a nearby ocean or sea with turning wind shear and dry air in the mid

https://doi.org/10.1017/9781009485654.012 Published online by Cambridge University Press

troposphere, giving rise to high CAPE values. The African maxima in hail probability coincide with areas that experience strong MCSs (Laing and Fritsch, 1997). In Switzerland, the frequency of convective storms is highest in the pre-alpine regions (Feldmann et al., 2023), highlighting the importance of some orographic lifting for convective storm initiation. Note that there are considerable uncertainties in the global frequency of hail (Prein and Holland, 2018; Raupach et al., 2021), because hail can not be reliably obtained from satellite remote sensing observations. Lightning observations, on the contrary, can be obtained from satellite remote sensing and agree reasonable well with ground observations, especially for longer flash durations (Poelman and Schulz, 2020).

11.5 Tropical Cyclones

TCs are among the most intense and devastating storms with roughly 80 TCs occurring per year worldwide (Ramsay, 2017). They range in diameter from 100 km to well over 1000 km[19]. TCs belong mainly to the meso-α scale but can extend into the lower end of the synoptic scale (Figure 1.24). The largest TCs occur in the northwestern Pacific Ocean. Typhoon Tip in 1979 still holds the record for being the largest TC with a diameter of 2200 km (Choy et al., 2015).

11.5.1 General Characteristics

As the name suggests, TCs develop in the tropics. A TC is characterized by a cloudless eye in its center, as illustrated in Figure 11.23. The eye typically ranges between 30 and 65 km in diameter, but diameters between 7 and 90 km[20] have also been observed[21]. The eye is surrounded by the eyewall, in which the most vigorous convection with thunderstorm activity occurs. However, convection is not restricted to the eyewall but also exists further away from the center of the TC, where it occurs in bands that are separated by areas of descending motions (Figure 11.23). These rainbands are caused by symmetric instability (Figure 4.10). The highest wind speeds near the surface are found underneath the eyewall. The maximum sustained wind speed over 1 min at 10 m above ground is used to categorize the intensity of TCs according to the Saffir–Simpson scale[22] (The Hurricane Disaster—Potential Scale, 1974), which has five categories (Table 11.2). TCs in category 5 are the most severe, with wind speeds exceeding 250 km h^{-1}.

The most intense TC in terms of 1-min sustained windspeed was Hurricane Patricia[23] in the northeast Pacific basin in 2015 with 346 km h^{-1}. The storm surge and minimum pressure values listed in Table 11.2 are for reference only, as some weaker TCs can cause a large storm surge depending on the bathymetry and the tide and vice versa.

TCs have different names depending on the ocean basin in which they form. TCs formed in the north Atlantic, the northeast Pacific east of the dateline, and the south Pacific east of

[19] https://glossary.ametsoc.org/wiki/Tropical_cyclone
[20] https://wmo.asu.edu/content/tropical-cyclone-smallest-eye,https://wmo.asu.edu/content/tropical-cyclone-largest-eye
[21] www.aoml.noaa.gov/hrd-faq/#tc-components
[22] www.nhc.noaa.gov/aboutsshws.php
[23] www.aoml.noaa.gov/hrd-faq/#record-setters

https://doi.org/10.1017/9781009485654.012 Published online by Cambridge University Press

Table 11.2 Saffir–Simpson scale of TC intensity. The categories are based solely on the maximum wind speed sustained over 1 min at 10 m above ground. Typical storm surge and minimum pressure values for each category are listed as well.

TC	Maximum wind speeds ($m\,s^{-1}$ ($km\,h^{-1}$))	Storm surge (m)	Minimum pressure (hPa)
1	33–42 (119–153)	1.0–1.7	980–994
2	43–49 (154–177)	1.8–2.6	965–979
3	50–58 (178–208)	2.7–3.8	945–964
4	59–69 (209–251)	3.9–5.6	920–944
5	$\geq$ 70 (252)	$\geq$ 5.7	$\leq$ 920

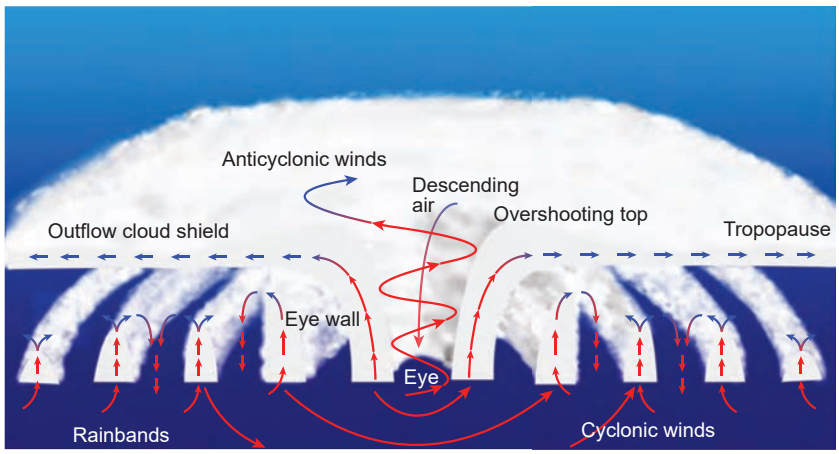


Figure 11.23 Schematic of the three-dimensional structure of a TC on the Northern Hemisphere. The solid arrows at the surface denote the primary circulation; in the eye, the downward arrow indicates the subsidence and the upward circulating arrow indicates the change in rotation axis from the surface to the top. The short red and blue arrows denote the rising and sinking air and the short blue arrows denote the outflow at cloud top.

160 °E are called *hurricanes*. TCs that form in the northwestern Pacific west of the dateline are called *typhoons*. In all other basins, TCs are called *tropical cyclones*[24] (Figure 11.24).

The seasonality of TCs in the different basins (see Figure 11.24) is largely determined by the seasonal cycle of the Sea surface temperature (SST). Only the North Indian ocean has two TC seasons, preceeding and following the Indian summer monsoon (April to June and October to December). The northwestern Pacific can produce TCs all year, although TCs are least likely in February and March (Ramsay, 2017).

[24] www.metoffice.gov.uk/weather/learn-about/weather/types-of-weather/hurricanes/location

https://doi.org/10.1017/9781009485654.012 Published online by Cambridge University Press

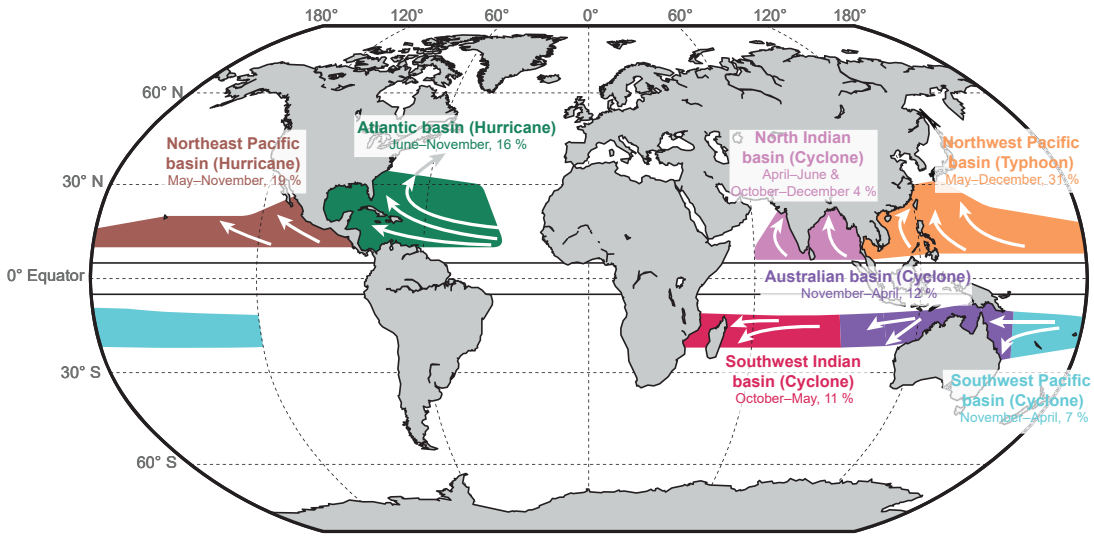


Figure 11.24 Schematic of the frequency of occurrence of tropical cyclones. The colored areas depict the approximate regions where TCs are typically observed within each basin. Also indicated for each basin is the typical season of TC occurrence based on Ramsay (2017). The numbers indicate the percentage of TCs occurring in each basin relative to the global total frequency of occurrence for data between 1990 and 2014 (Ramsay, 2017).

11.5.2 Prerequisites for Tropical Cyclone Formation

The conditions necessary for TC formation have been extensively studied (Gray, 1968; Emanuel, 2003; Menkes et al., 2012; Lin et al., 2022). In general, there are six pre-requisites for a TC to form. These can be divided into three thermodynamic criteria (i–iii) and three dynamic criteria (iv–vi) (Gray, 1968).

(i) The ocean thermal energy as measured by the SST needs to be sufficiently high (Gray, 1968), because evaporation of water from the ocean surface provides the energy for a TC. It was found that 98 % of all TCs between 1981 and 2008 formed when the SST was higher than 26.5 °C (Tory and Dare, 2015). As the strong winds associated with a TC stir up colder water from lower levels in the ocean, the water down to a depth of at least 50 m needs to be sufficiently warm. A shallower mixed-layer depth may cause cold water to be stirred up, which could limit or even cut off the energy supply of the TC.

(ii) The mid-troposphere needs to be sufficiently moist. This is because otherwise entrainment of dry air could prevent convective clouds from rising all the way to the tropopause.

(iii) The moisture flux at the ocean–air interface needs to be sufficiently high to sustain a conditionally unstable thermodynamic environment (Montgomery and Smith, 2017).

(iv) The formation must occur $>5°$ away from the equator, explained as follows: The word "cyclone" suggests that a TC is a rotating storm system. The Coriolis force is required to initiate rotation of the moving air masses and it is only strong enough $>5°$ away from the equator. Note that the Coriolis force is negligible for the rotations in convective storms and tornadoes (Section 11.2.5) because of their smaller horizontal extents and much shorter lifetimes.

https://doi.org/10.1017/9781009485654.012 Published online by Cambridge University Press

(v) The vertical wind shear should not be too strong because otherwise it would tear off the tops of the convective clouds. Such erosion of the overcasting clouds would allow more infrared radiation to be emitted to space, which would cool the core and weaken the storm. Vertical wind shear also tilts the TC, causing heat and moisture to be removed from the center of the TC. Also, vertical wind shear enables dry low-energy air from the environmental mid troposphere to enter the storm, further weakening it (Riemer et al., 2010). Nonetheless, analysis of the vertical wind shear in 139 developing depressions has been found to be 10.5 ± 4.8 m s^{-1}, suggesting that some weak vertical wind shear is beneficial for tropical cyclogenesis to create synoptic-scale ascent (Bracken and Bosart, 2000). All together, the TC becomes a less efficient heat engine (Section 11.5.5) in the presence of strong vertical wind shear.

(vi) There must be an initial disturbance. This disturbance can lie in the tropics or be of extratropical origin (Dunkerton et al., 2009). Most common are tropical disturbances, examples of which include equatorial Rossby waves, moist Kelvin waves, or tropical easterly waves (Dunkerton et al., 2009). The process by which a TC originates from an extratropical disturbance is called *tropical transition*, which is especially important in the North Atlantic, where almost 40 % of all TCs originate from an extratropical disturbance (McTaggart-Cowan et al., 2013). Examples for extratropical disturbances are breaking Rossby waves and streamers of potential vorticity (Galarneau et al., 2015; Enz et al., 2023).

Here we focus on discussing TC formation via tropical easterly waves, which initiate the majority of TCs in the Atlantic and eastern Pacific sectors (Dunkerton et al., 2009). A tropical easterly wave is a north–south-oriented elongated area of high vorticity and relatively low pressure that travels from east to west in the tropics. It has its origin in the ITCZ (Figure 1.1). The most prominent example is provided by *African easterly waves* (AEWs) (e.g., Burpee, 2003). AEWs are westward-propagating, large-scale (synoptic) wave perturbations (2000–4000 km) (Hsieh and Cook, 2005), which during the summer seasons can transit the Atlantic from West Africa to the Caribbean, as initially described in detail by Carlson (1969). They appear as continuous wave trains with a period of approximately 3–5 days (Hsieh and Cook, 2005) that originate over North Africa from instabilities in the *African easterly jet* (AEJ). The mid-tropospheric AEJ forms as a result of the strong temperature and moisture gradient between the hot and dry Sahara in the north and the cooler Atlantic ocean to the south (Cook, 1999). To remain in thermal wind balance (Section 4.6.5), the atmosphere develops a strong vertical wind shear, which causes the low-level winds to reverse their direction and flow eastward as part of the African monsoon circulation. The AEJ itself flows toward the west.

The instabilities within the AEJ have long been recognized to form the seed circulation for a tropical easterly wave. In fact, in the Atlantic, almost 60 % of all tropical storms and more than 80 % of intense hurricanes ($\geq$ category 3 on Saffir–Simpson scale) have been found to develop from AEWs (Erickson, 1963; Landsea, 1993), as shown in Figure 11.25.

A surface low-pressure region travelling on the equatorwards side of a tropical wave, where lots of moisture is available, provides the ideal place for TC genesis because it (i) provides a region of cyclonic vorticity and convergence, (ii) contains a lot of moisture that can get lofted by the deep convection, (iii) confines the convective storms so that they can aggregate and (iv) maintains or even enhances the parent wave until the vortex becomes self-sustained and emerges from the wave as a tropical depression (Dunkerton et al., 2009). This sheltered

https://doi.org/10.1017/9781009485654.012 Published online by Cambridge University Press

environment is also termed "pouch", in analogy to the pouch where female kangaroos carry their babies (Dunkerton et al., 2009), because it is protected from entrainment of dry environmental air and hence preserves the moisture (Bretherton et al., 2005). Thus, the pouch is an ideal place for non-rotating convective clusters to gain vorticity and to develop synoptic-scale cyclonic circulation features that can potentially develop into a TC. In other ocean basins, sources for cyclonic vorticity and convergence are provided by the ITCZ or by monsoon troughs (e.g., Chia and Ropelewski,2002).

11.5.3 Lifecycle and Lifetime of TCs

Overall, the formation of a TC can roughly be understood as three stages, as shown in Figure 11.25 for a TC in the Atlantic basin, developed from a disturbance off the West coast of North Africa, near theCape Verde islands.

First, a cluster of convective storms forms, termed a *tropical disturbance*. While clusters of convective storms can be found in many places in the tropics, only a fraction of them can gain vorticity and convergence to form so-called *TC seeds* (e.g., Hsieh et al., 2020; Emanuel, 2022). This requires that the cluster of convective storms is, for example, embedded in a tropical easterly wave. At this stage, the tropical disturbance does not have a closed wind circulation[25]. Sources of this disturbance include AEWs, as discussed earlier. This initial disturbance is classified as a tropical depression, if at least one closed isobar around a low pressure centerexists.

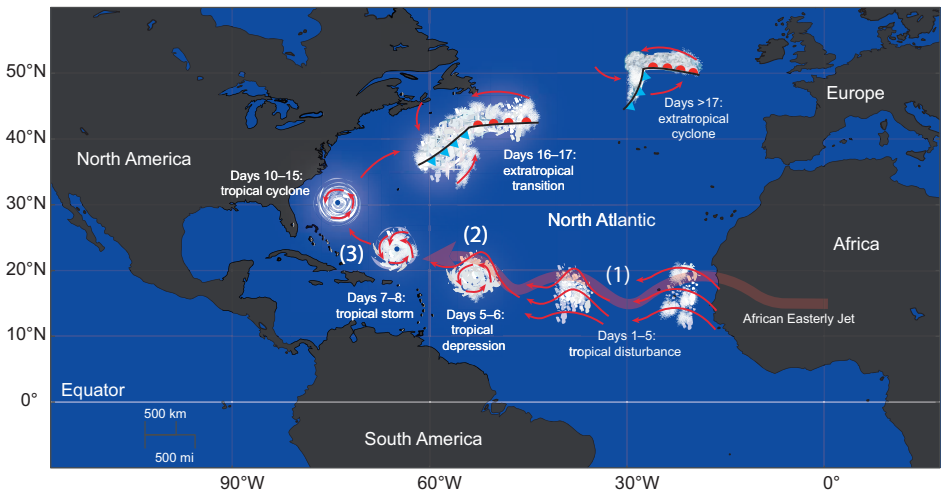


Figure 11.25 Schematic of a typical life cycle of a TC in the North Atlantic forming off the West coast of North Africa, near the Cape Verde Islands. The three characteristic stages of TC formation include (1) tropical disturbance forming in an African Easterly Wave, (2) tropical depression, and (3) self-sustained tropical storm, and are followed by extratropical transition of the TC. See text for details. The red arrows denote the circulation in the planetary boundary layer.

[25] https://glossary.ametsoc.org/wiki/Tropical_disturbance

https://doi.org/10.1017/9781009485654.012 Published online by Cambridge University Press

In our example, the tropical depression forms equatorwards of the AEJ. In a tropical depression, the wind speeds reach values up to 17 m s^{-1}. From this stage onward, the different stages of the convective storm are distinguished based on the maximum wind speed that is sustained for 1 min.

Second, a self-sustaining tropical, convective storm develops from this tropical depression, as the wind speeds intensify, reaching values of 17–33 m s^{-1} [26].

Third, further development and clustering of the convective storm produce a cyclone. This cyclone is characterized by an almost axis-symmetric structure and a cloud-free center, with wind speeds exceeding 33 ms^{-1}. Depending on the maximum sustained wind speed, a TC is then classified by the Saffir–Simpson wind scale[27] (Table 11.2).

The approximate time spans for each stage of TC formation are indicated in the example shown in Figure 11.25. We note that the reported lifetimes of a TC, as archived in the Atlantic best-track hurricane data base HURDAT[28], only include the tropical storm and TC stages. The lifetime of a TC is highly variable: while the average lifetime of an Atlantic hurricane is 7–9 days (Enz et al., 2023), the record lifetime was 31 days[29]. As the TC travels polewards and reaches midlatitudes, it gradually loses TC characteristics and becomes more extratropical in nature (Figure 11.25) as will be discussed in Section 11.5.6.

11.5.4 Circulation Within a Tropical Cyclone

The circulation of a fully-developed TC can be divided into a dynamic contribution, the primary circulation, and a thermodynamic contribution, the secondary circulation. Together they result in a air parcel trajectory constituting an in-up-and-out circulation, termed the overturning circulation of a TC, as described next.

Primary Circulation

The *primary circulation* comprises horizontal spiralling winds, that is, the general axis-symmetric rotation of the TC, as shown in Figure 11.26a. It can be described by the gradient wind balance (eq. 4.48), which describes the balance between the Coriolis, pressure gradient, and centrifugal forces (Section 4.6.1). As illustrated in Figure 11.26b, the pressure is lowest in the eye of the TC, but the tangential wind speed (eq. 11.11) has its maximum underneath the eyewall. These strong tangential wind speeds close to the core can mostly be understood from the conservation of angular momentum. An example of conservation of angular momentum is an ice skater who contracts their arms toward the body: when r decreases, v_t must increase accordingly (neglecting the Coriolis term in eq. 11.10), that is, the ice skater spins faster. Likewise, in a TC, the frictional-induced inflow causes r to decrease, hence v_t increases until its maximum is reached underneath the eyewall (Figure 11.26). This is a simplified explanation because some angular momentum is destroyed by friction in the planetary boundary layer.

[26] www.nws.noaa.gov/directives/.
[27] www.nhc.noaa.gov/climo/#overview
[28] www.nhc.noaa.gov/data/#tcr
[29] https://wmo.asu.edu/content/tropical-cyclone-longest-lasting-tropical-cyclone

https://doi.org/10.1017/9781009485654.012 Published online by Cambridge University Press

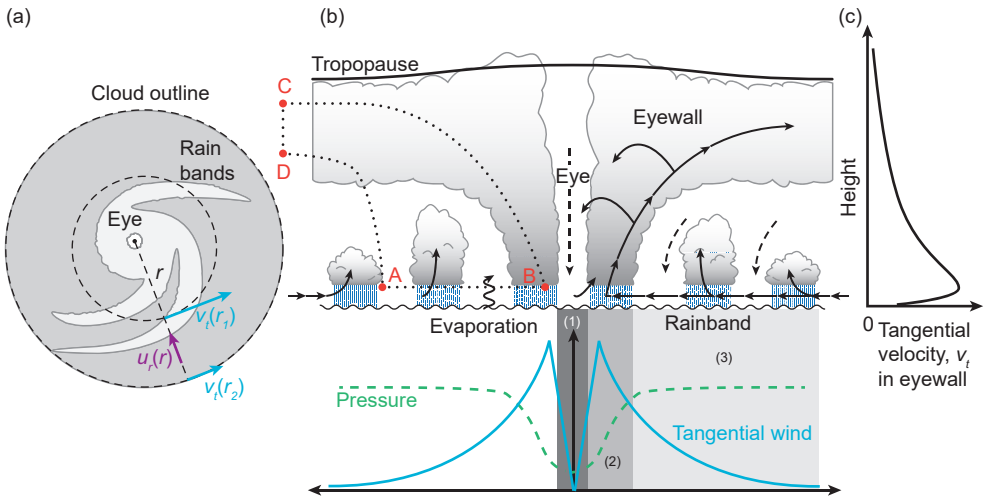


Figure 11.26 Schematic of (a) the primary circulation viewed from above and (b) the overturning circulation in a cross section of a TC. The different regions in a TC are indicated by numbers: (1) refers to the eye, (2) to the eyewall, and (3) to the outer region. The letters A-D denote the different stations in the Carnot process (Figure 11.28), which is often used to describe the energy conversion associated with the overturning circulation of a TC. The distributions of pressure (dashed green line) and tangential wind (solid blue line) near the surface of a TC as a function of radius are qualitatively shown in the lower part of panel (b). Panel (c) shows how the tangential wind speed v_t changes with altitude in a TC.

Frictional-Induced Inflow

To visualize the frictional-induced inflow into a TC, imagine stirring a cup of tea made with tea leaves. If you stop stirring, the tea leaves accumulate in the center, because of frictional convergence and gravity. The same would happen to the air in a TC in the absence of the overturning circulation, because friction due to the ocean surface (waves) causes the inflow of boundary layer air to converge in the center.

Conservation of angular momentum m (eq. 11.10) can be assumed above the PBL. It implies that the tangential wind speed v_t is higher at smaller radii (Figure 11.27b). In the PBL, m is not constant because of friction. Here, a larger windspeed implies higher friction, which increases the subgradient wind (eq. 4.59) and hence the frictional-induced inflow into the TC. Even though some m is destroyed by friction, v_t is still increasing inward because the decrease in r is larger than the destruction of m by friction.

Approximately at the radius of maximum tangential wind speed (open black dots in all panels of Figure 11.27), friction cannot keep up with the increase in windspeed, so that the subgradient wind turns in a supergradient wind (eq. 4.60). In addition, the subsidence in the eye pushes the air in the boundary layer outward.

Convergence of Air and Ascent in the Eyewall

The convergence of the sub- and supergradient winds in the PBL causes the air masses to rise in the eyewall ("up"-component, Figure 11.27c). Without the formation of Cb clouds, and the

https://doi.org/10.1017/9781009485654.012 Published online by Cambridge University Press

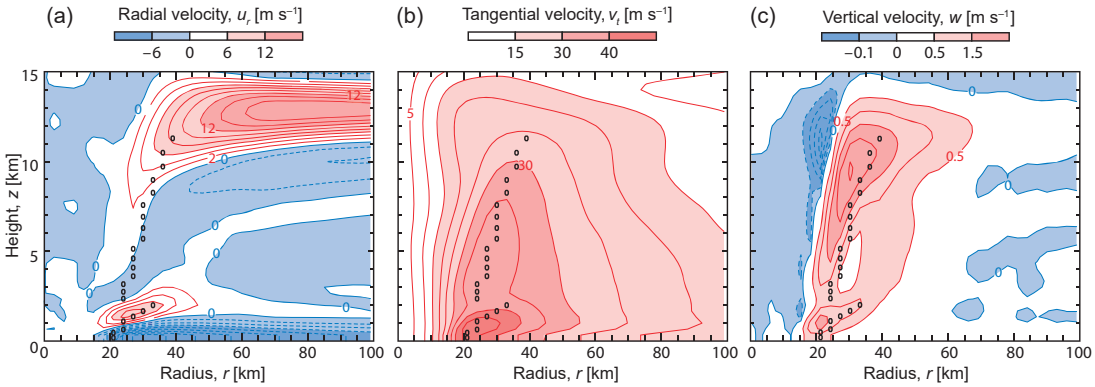


Figure 11.27 Radius-height cross sections of the azimuthally averaged velocity components in the simulation described by Persing et al. (2013), time averaged during an intensification phase of a 3D calculation: (a) radial velocity (contour interval 2 m s^{-1}), (b) tangential velocity (contour interval 5 m s^{-1}), and (c) vertical velocity (contour interval 0.5 m s^{-1} for positive values and 0.1 m s^{-1} for negative values). Solid contour lines denote positive values and dashed ones negative values. The open black circles in each plot show the location of the maximum tangential wind speed at each height. Figure adapted from Persing et al. (2013).

associated latent heat release in the eyewall, the TC circulation would be shallow, as seen by the supergradient outflow above the boundary layer in Figure 11.27a (red region of positive radial velocity between 1 and 3 km altitude).

Sawyer–Eliassen Circulation

The release of latent heat induces a so-called *secondary circulation* (Smith and Montgomery, 2024) or *Sawyer–Eliassen circulation* (Pendergrass and Willoughby, 2009), as visualized by the mid-level inflow of air into the eyewall between roughly 3 and 10 km altitude in Figure 11.27a (blue region of negative radial velocity). Mathematically, the Sawyer–Eliassen circulation describes a circulation that develops to restore thermal wind balance, which is broken by the local latent heating. The local heating causes a reduction in pressure followed by adiabatic expansion and cooling to balance this temperature increase (Montgomery and Smith, 2014). This reduction in pressure leads to the mid-level inflow both from outside and inside the eyewall and completes the Sawyer–Eliassen circulation.

Upper Level Outflow

The rising of the buoyant air within the eyewall mostly stops at the tropopause, which denotes an LNB, except for some overshooting. From there, the air masses spread out anticyclonically ("out"-component), forming the upper tropospheric outflow of a TC. This outflow corresponds to the positive radial velocity in Figure 11.27a. The outflow occurs in regions of symmetric instability, where the air is accelerated outward as can be seen in satellite images in the spiral cloud and rain bands.

https://doi.org/10.1017/9781009485654.012 Published online by Cambridge University Press

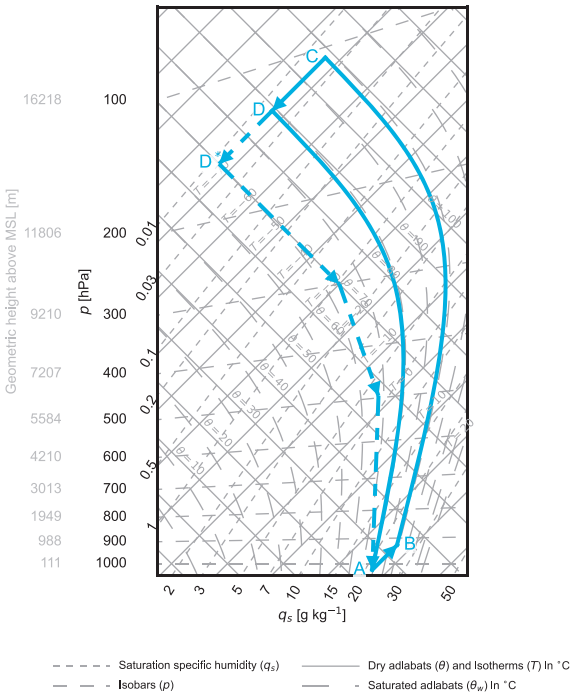


Figure 11.28 Overturning circulation of a major tropical cyclone depicted as a Carnot cycle in a tephigram. Points A–D are labeled according to Figure 11.26.

Formation of the Warm Core

Due to mass continuity, not all of the air spreads out anticyclonically, rather some is pushed into the center of the TC and forced to subside within the eye (Figure 11.27c). The warm core is mainly caused by the advection of latent heating from the eyewall to the center of the TC (Ohno and Satoh, 2015). The warm core is further enhanced by adiabatic compression of the sinking air in the eye. The warm core in turn causes a high-pressure anomaly at upper levels, going along with decreasing tangential wind speeds with increasing altitude (Figure 11.26c and Figure 11.27b).

Overturning Circulation

The *overturning circulation* describes the combination of the radial, frictional-induced inflow, vertical rise in the eyewall, radial outflow, and subsidence of air masses in the outer region of the TC. It is also called the *in-up-and-out circulation*, as is illustrated in Figure 11.26b. Inflow and convergence of boundary layer air at lower levels ("in"-component) is shown by the negative radial velocities in Figure 11.27a, denoting a subgradient wind (eq. 4.59). The "up"-component is best seen in Figure 11.27c, with the eyewall sloping outwards with increasing altitude. This is a result of m being conserved above the boundary layer in the ascending eyewall air and v_t decreasing with altitude, which requires the radius of the eye to increase with increasing altitude. The "out"-component is shown by the positive radial velocities below the tropopause in Figure 11.27a, denoting a supergradient wind (eq. 4.60). The overturning circulation is closed by the weak subsidence outside the eyewall (Figure 11.27c). Because all

https://doi.org/10.1017/9781009485654.012 Published online by Cambridge University Press

aspects of the TC circulation contribute to the overturning circulation, a strengthening of any of them (primary circulation, frictional induced inflow, mid-level inflow) implies a stronger overturning circulation and vice versa.

11.5.5 Tropical Cyclone as a Carnot Heat Engine

The overturning circulation of a TC converts thermal energy from the ocean into kinetic energy and mechanical work. This process can be described as a Carnot cycle (Section 3.2.5 and Emanuel, 1986). In general, heat engines transfer energy from a warm to a cold region and by doing so, convert some of that heat energy to mechanical work (Figure 3.7a). In a TC, the low pressure at its center initially causes strong surface winds in the form of inflowing boundary layer air, which cause a flux of heat and moisture from the ocean to the atmosphere. The energy required for the isothermal expansion of the Carnot process (from A to B in Figures 11.26 and 11.28) is mainly provided in the form of latent heat from the evaporation of water from the ocean. Because the energy of the evaporated water is stored in the form of water vapor, the temperature remains approximately constant during its inflow, but the equivalent potential temperature θ_e (eq. 3.108) increases. For the example in Figure 11.28, we assume an inflow temperature of 300 K as discussed earlier. The inflowing air expands owing to the decrease in pressure toward the TC center: in Figure 11.28, decreasing from 1000 to 900 hPa. Moist adiabatic expansion occurs when the air is lifted and the water vapor condenses during its ascent in the eyewall (from B to C in Figures 11.26 and 11.28). This ascent closely follows a constant θ_e surface. During the ascent, the temperature decreases from 300 K at the cloud base to about 200 K at the tropopause, where the ascent terminates. In the periphery of the TC at point C, the air sinks because of clear-sky radiative cooling. As this radiative cooling is balanced by warming due to adiabatic compression, the temperature remains approximately constant until point D. Connecting the Carnot cycle with the discussion in Section 3.2.5, one can also understand the process of isothermal compression the opposite way around: Mechanical work is needed for compression, part of which is transformed to heat (Figure 3.7b, step $3 \rightarrow 4$). In the case of the TC, this heat is radiated off by emission of longwave radiation from air molecules at the periphery of the TC. Between D and A, the air warms due to adiabatic compression and the cycle is closed (Figures 11.26 and 11.28). Whereas in an idealized Carnot cycle the adiabatic compression also needs to strictly follow a θ_e surface back down again, in reality the descending air will follow a path between a dry and saturated adiabat, as shown by the broken arrows from D* to A in Figure 11.28. Further, we note that some of the air masses rising within the eyewall do not get transported to the periphery of the outflow cloud shield, but sink within the eye.

The efficiency of a Carnot cycle in which heat energy is converted into mechanical work can be obtained from the difference between the temperature at which thermal energy is put into the system, T_{in}, and the temperature at which energy leaves the system, T_{out}, divided by the input temperature (eq. 3.37). In the case of a TC, T_{in} corresponds to the cloud base temperature, which can be approximated as SST - 5 K (Emanuel, 1986). For simplicity, let us take $T_{in} = 300$ K and T_{out} as the temperature at the tropopause T_{tropo} (approximately 200 K), which results in an efficiency η of approximately one third:

https://doi.org/10.1017/9781009485654.012 Published online by Cambridge University Press

$$\eta = \frac{T_{in} - T_{out}}{T_{in}} \approx= \frac{300 - 200}{300} = \frac{1}{3}. \tag{11.14}$$

This means that approximately one third of the heat energy in a TC is converted into mechanical work (Figure 3.7a). This work occurs as the acceleration work, or kinetic energy, in the form of high horizontal wind speeds driving the primary circulation of the TC, which may cause major damage when the TC makes landfall.

An estimate of the maximum windspeed in a TC can be related to its Carnot efficiency by assuming that the TC is in a steady state, where the rate of generation of available heat energy G_e equals its mechanical dissipation D_e (Emanuel, 1986, 1995). G_e is the sum of the latent and sensible heat fluxes:

$$G_e = \eta C_k \rho_a v_{t,s}(k_s^* - k_B), \tag{11.15}$$

where C_k is the enthalpy transfer coefficient and $v_{t,s}$ is the tangential wind speed at the surface. Moreover, k_s^* and k_B denote the enthalpies at the ocean surface (saturated) and at cloud base (point B in Figure 11.28). Thus, a higher $v_{t,s}$ implies larger G_e and θ_e, a colder T_{out}, a higher Carnot efficiency η, and a more severe TC. The rate of mechanical dissipation D_e of the kinetic energy depends highly on tangential wind speed, being proportional to $v_{t,s}^3$. D_e also depends on the roughness or drag exerted by the ocean surface (waves), described by the drag coefficient C_D:

$$D_e = C_D \rho_a v_{t,s}^3. \tag{11.16}$$

In equilibrium, $G_e = D_e$. We now evaluate these quantities for the maximum tangential windspeed $v_{t,max}$ at the radius of the maximum wind speed r_{max} and obtain:

$$v_{t,max}^2 = \frac{C_k}{C_D} \eta (k_s^* - k_B)\Big|_{r_{max}}. \tag{11.17}$$

11.5.6 Decay of Tropical Cyclones

The main source of energy for TCs is the latent heat delivered by the warm ocean due to evaporation. This energy supply can be cut off if the TCs make landfall, move over colder ocean waters, or undergo extratropical transition. If the heat source is cut off, the TC decays very rapidly. If landfall occurs over a swamp, the TC can still pick up some heat energy to slow its dissipation (Emanuel, 2005*b*). However, if the TC encounters high surface roughness after landfall, for instance, due to orography, its decay can be even more rapid because of increased frictional loss of kinetic energy (Kaplan and DeMaria, 2001).

Upon landfall, TCs cause serious damage with many casualties. Most damage is associated with storm surges (Table 11.2), that is, the increase in sea level, which can flood coastal communities. The storm surge is worse when it coincides with high tides. A record storm surge of 9 m was recorded in 1899 for TC Mahina, hitting Bathurst Bay in Australia[30].

The horizontal wind speeds are highest on the right quadrant with respect to the motion of the TC on the Northern Hemisphere due to the superposition of translational and rotational winds. The horizontal wind speed decays exponentially when TCs hit land (Kaplan and

[30] www.aoml.noaa.gov/hrd-faq/#record-setters

https://doi.org/10.1017/9781009485654.012 Published online by Cambridge University Press

DeMaria, 1995). Rainfall also diminishes after landfall, but not as fast as the horizontal wind speed because the TC still contains a lot of water vapor that can condense when it moves over land.

About 50 % of North Atlantic and northwestern Pacific TCs undergo extratropical transition (Hart and Evans, 2001; Bieli et al., 2019). Extratropical transition occurs when TCs move polewards and connect with the midlatitude upper-level flow (Figure 11.25). This transition mostly occurs between 35 and 45 ° latitude (Hart and Evans, 2001). During the extratropical transition, the cyclone typically loses its symmetric warm core by reversal of the thermal wind gradient into the center and becomes a cold core system (Evans et al., 2017). The cold core implies that the low pressure, and thus the winds, strengthen with height. As the low-pressure center at the surface is typically ahead of an upper-level trough, the cyclone center tilts backwards in the direction of the large-scale flow with increasing height (Figure 11.29f). The cyclone also gains asymmetry by developing fronts, in which the warm air pushes polewards and the polar air pushes equatorwards.

After an extratropical transition, the main energy source no longer is the evaporation of water from the ocean, but rather the horizontal temperature contrast, which causes baroclinic instability (Jones et al., 2003). The extratropical cyclone can increase in size and can also re-strengthen due to baroclinic instability after it has undergone extratropical transition (Hart and Evans, 2001).

Hurricane Sandy underwent extratropical transition on October 29, 2012, when making landfall in New Jersey and hitting New York City. Hurricane Sandy intensified as it made landfall, with contributions from both tropical and baroclinic energy sources (Evans et al., 2017). It started to become slightly asymmetric early on while still keeping its eye and increasing in strength. Hurricane Sandy developed a warm core seclusion as the cold continental air encircled the warm core vortex (Galarneau et al., 2013). Upon landfall, the central pressure quickly increased and the warm core weakened. The polar jet stream extended rather far to the south, enabling Hurricane Sandy to interact with the upper-level trough during its extratropical transition (Galarneau et al., 2013).

11.5.7 Differences between Tropical and Extratropical Cyclones

The major differences between tropical and extratropical cyclones, also referred to as midlatitude cyclones, are visualized in Figure 11.29. An extratropical cyclone is caused by baroclinic instability (Section 4.6.5), by instability due to intersecting isobars and isotherms. In contrast, a TC receives its energy from the evaporation of warm ocean water and the associated latent heat release in the eyewall.

Both tropical and extratropical cyclones rotate cyclonically near the surface. However, one distinct difference between the two cyclone types is that a TC has a warm core, whereas an extratropical cyclone has a cold core. A warm core causes the pressure minimum to weaken with height, according to the hypsometric equation (4.15), until the pressure gradient vanishes in the mid-troposphere (Figure 11.29e). At higher levels, the circulation reverses, such that the outflow at upper levels is anticyclonic (Figure 11.23). In contrast, an extratropical cyclone has

https://doi.org/10.1017/9781009485654.012 Published online by Cambridge University Press

a low-pressure anomaly throughout its vertical extent and a cold core in higher levels (Figure 11.29f). Therefore the air rotates cyclonically at all altitudes in an extratropical cyclone. In fact, because of the cold core, the pressure anomaly increases with height in an extratropical cyclone, again according to the hypsometric equation (4.15), which causes the highest wind speeds to be located in the upper troposphere. Furthermore, a TC is symmetric, allowing the eye of the TC to be visible, whereas the center of an extratropical cyclone tilts backwards with height (not symmetric).

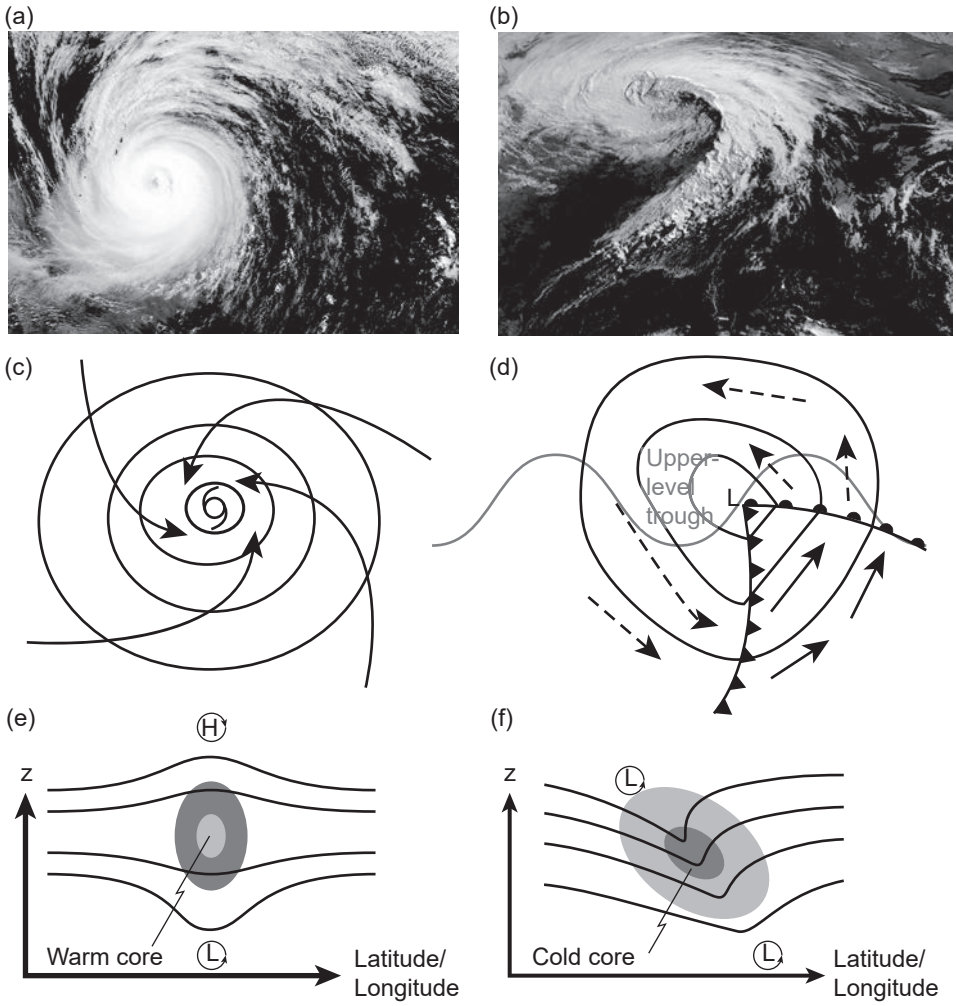


Figure 11.29 Satellite pictures (top panels) and schematics of a TC (a), (c), (e) and an extratropical cyclone (b), (d), (f). The middle panels are schematic views of the surface circulation as seen from above. The solid arrows denote the flow of warm air masses and the broken arrows denote cold air masses. The solid lines are isobars. The bottom panels show cross sections of latitude or longitude versus height along a line going through the center of the cyclones. Image credits: (a) NOAA Goddard MODIS Rapid Response Team and (b) NOAA image gallery.

https://doi.org/10.1017/9781009485654.012 Published online by Cambridge University Press

Some cyclones have characteristics of both tropical and extratropical cyclones. These so-called *Medicanes* occur in the Mediterranean Sea. They often originate as an extratropical cyclone and then transition into a cyclone with tropical characteristics (e.g., Emanuel, 2005*a*; González-Alemán et al., 2019). They occur very seldomly, on average once every two years (Tous and Romero, 2013).

11.6 Severe Convective Storms and Tropical Cyclones in a Warming Climate

It is projected that the average and maximum rain rates associated with extratropical cyclones and severe convective storms will increase in a warming climate, due to the increases in atmospheric water vapor (Seneviratne et al., 2021). CAPE is projected to increase in response to global warming due to the steepening of moist adiabats in the warmer climate. This increases the locations with favorable environments for severe convective storms, lengthens the severe convective storm season in the United States (Seneviratne et al., 2021) and enhances convective activity in high latitudes (Chen et al., 2021; Poujol et al., 2021).

How hailstorms change in the future is still uncertain because of limited observational evidence. More intense hailstorms could be expected as low-level moisture and convective instabilities increase, which promotes the formation of larger hailstones within convective storms. On the other hand, global warming has already led to an increase in the average melting-level height of 3.2 ± 1.4 m yr^{-1} (Prein and Heymsfield, 2020; Raupach et al., 2021). This is expected to continue, such that more hailstones will melt between that level and Earth's surface. Thus, only the larger hailstones within a cloud will survive when falling toward Earth's surface, as shown for a 3 °C warmer Europe (Thurnherr et al., 2025). There is a large regional variability in the decrease or increase in the number of hail days of differently sized hailstones across Europe (Thurnherr et al., 2025). This variability is also seen worldwide. Raupach et al. (2021) concluded that the frequency of hail at Earth's surface is expected to slightly increase in Europe and Australia, and to decline in East Asia and North America, depending on how the vertical wind shear, CAPE, CIN, and melting level height change in these regions (Raupach et al., 2021).

In general, projections about future changes in hazards associated with convective storms (tornadoes, hail, and lightnings) remain highly uncertain. For instance, projections about changes in lightning flash density range between a 45 % increase to a 7 % decrease in a 3.4 K warmer climate (Clark et al., 2017). This large uncertainty related to future changes in extremes is partly caused by climate models not having a sufficiently high horizontal resolution to resolve deep convection (Seneviratne et al., 2021). This will change, as more and more climate simulations will be conducted at convection-permitting horizontal resolution, that is, with grid spacings below 5 km (Fosser et al., 2024). Additionally, the observational record is inhomogeneous and sparse complicating climate change attribution assessments.

Whether, and in what ways, TCs have changed and will change over time is a research subject of considerable interest (e.g., Pielke et al., 2005; Webster et al., 2005; Walsh et al., 2016). Establishing robust, long-term trends of TC occurrence is challenging because the capabilities

https://doi.org/10.1017/9781009485654.012 Published online by Cambridge University Press

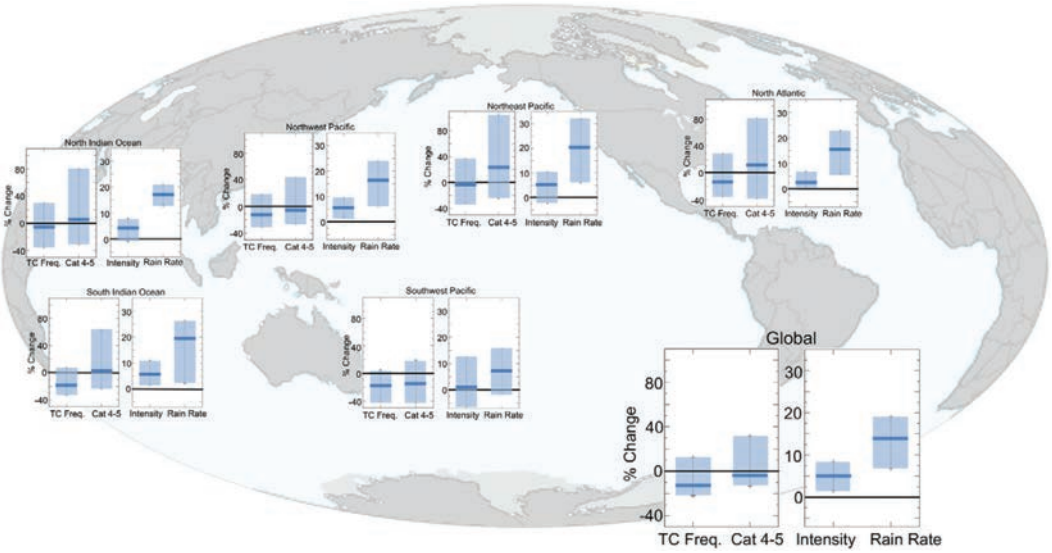


Figure 11.30 Projections of TC characteristics for a 2 °C global warming scenario (Knutson et al., 2020). Shown globally and for each basin are median and percentile ranges for projected percentage changes in TC frequency, categories 4–5 TC frequency, TC intensity, and TC near-storm rain rate. For TC frequency, the 5th–95th-percentile range across published estimates is shown. For categories 4–5 TC frequency, TC intensity, and TC near-storm rain rates, the 10th–90th-percentile ranges are shown. Note the different vertical axes. ©American Meteorological Society. Used with permission.

for observing cyclones over the oceans were rather limited before the usage of weather satellites in the 1970s (Knutson et al., 2019). Increasing SSTs provide more energy for TCs in a warmer climate, but the evaluation of the changes in all six prerequisites for TC formation (Section 11.5) is necessary to fully understand and project the changes in TC frequency and intensity in a warmer climate. This is further complicated due to the possible influence of interannual and decadal natural variability, such as the El Niño/Southern Oscillation circulation or the Atlantic multidecadal oscillation (Klotzbach, 2011). While globally no significant trend in TC frequency could be observed in recent decades, it is likely (occurrence probability is 66–100 %) that the global proportion of category 3-5 TCs and the TC intensity has increased over the past four decades (Kossin et al., 2020; Seneviratne et al., 2021). Other studies reported a decreasing trend of annual TC numbers during the 20th century (Chand et al., 2022).

Future projections of TC frequency and intensity hinge on the quality and horizontal resolution of GCMs and on uncertainties in climate change scenarios. The horizontal resolution of GCMs has increased in recent decades, so that by now medium to high-resolution (with horizontal resolutions as high as 16 km at the equator) multi-model ensemble simulations have been conducted and can be evaluated for changes in TC frequency (Yamada et al., 2021). These studies found that the TC frequency will decrease over time in the first half of the twenty-first century because of a decrease in TC genesis frequencies. At the same time, the average and maximum rain rates and the peak wind speeds from the most intense TCs will increase in a warmer climate (Seneviratne et al., 2021).

https://doi.org/10.1017/9781009485654.012 Published online by Cambridge University Press

The effect of climate change on TC characteristics for the different ocean basins is shown in Figure 11.30 (Knutson et al., 2020). In all ocean basins, the rain rate and TC intensity increase in a warmer climate. This is a consequence of enhanced evaporation from the ocean surface, leading to a higher water vapor content of the atmosphere according to the Clausius–Clapeyron equation (3.70). Thus, the specific humidity at a given RH is higher in a warmer climate and so is the cloud water content and the resulting precipitation rate. Differences exist in the overall TC frequency per basin and the frequency of the most intense TCs (categories 4 and 5). While the median values in the overall change in TC frequency in all ocean basins are slightly negative, consistent with the synthesis by IPCC AR6 (Seneviratne et al., 2021), the individual estimates are mixed and encompass a large uncertainty. Similarly, the most intense TCs (categories 4 and 5) are projected to increase in some ocean basins and to decrease in others (Knutson et al., 2020).

https://doi.org/10.1017/9781009485654.012 Published online by Cambridge University Press